MCMASTER UNIVERSITY

Methods for Performance Evaluation of the Acquisition Hardware for Microwave Imaging

Kaveh Moussakhani

A Thesis
Submitted to the Department of Electrical and Computer Engineering
and the School of Graduate Studies
of McMaster University
in Partial Fulfillment of the Requirements
for the Degree of
Doctor of Philosophy

DOCTOR OF PHILOSOPHY (2014) McMASTER UNIVERSITY
(Electrical and Computer Engineering) Hamilton, Ontario

TITLE: Methods for Performance Evaluation of the Acquisition Hardware for Microwave Imaging

AUTHOR: Kaveh Moussakhani
M.Sc.
Amirkabir University of Technology
(Tehran Polytechnic)

SUPERVISOR: Natalia K. Nikolova, Professor
Ph. D.
(University of Electro-Communications)
IEEE Fellow
P. Eng. (Ontario)
Canada Research Chair in High Frequency Electromagnetics

NUMBER OF PAGES: XI, 139

Abstract

This thesis contributes to the methods for evaluating the hardware performance of microwave imaging systems. Different aspects of this performance study are systematically described and evaluated through existing and novel performance metrics. The dynamic range of two vector network analyzers and their noise floor are explored. The effects of low noise amplifiers on the dynamic range of the microwave system are also studied. To increase the dynamic range and sensitivity of the system, a new high efficiency ultra wide band TEM horn antenna is introduced. The new antenna significantly blocks the electromagnetic interference from the surrounding medium. The parasitic coupling between the transmitting and receiving antennas has been reduced to a minimum. To estimate the efficiency of the antenna used in tissue imaging more realistically, a measurement based method is also proposed. The method models the two-port network formed by the antennas and the medium between them by signal flow graph. The medium's electrical properties mimic those of tissue and can vary according to the application. Also, a new performance metric for microwave systems namely, the physical contrast sensitivity is proposed. Methodologies are proposed for its evaluation through measurements and through simulations. This enables the estimation of the smallest detectable target permittivity contrast or size for the system under evaluation.

Acknowledgments

It would not have been possible to write this thesis without the help and support of the kind people around me, to only some of whom it is possible to give particular mention here.

First and foremost, I am thankful for my supervisor, Prof. Natalia Nikolova. This thesis would not have been plausible without her enormous help, support and patience, not to mention her advice and unsurpassed knowledge. I appreciate all her contributions of time, ideas and feedback to make my Ph.D. experience productive and stimulating. I am grateful for her support during the toughest times, which helped me to grow personally. I quite simply cannot imagine a better supervisor.

I would like to thank my co-supervisors and supervisory committee meeting members. I am grateful for Prof. John Bandler`s invaluable advice on presentation and impression which will help me through my entire carrier. I am thankful to Dr. Nagula Sangary, Dr. Aleksandar Jeremic and Matiar R. Howlader, for their precious time and valuable suggestions.

My colleagues in Computational Electromagnectis Laboratory have contributed immensely to my personal and professional time at McMaster. I am especially grateful to Dr. Reza Khalaj Amineh, for his valuable and genuine guidance and assistance; from antenna design and manufacture to writing the papers, to Sadegh Dadash and Ali Khalatpour, for their selfless collaboration during several projects, to Justin McCombe, for his meticulous experimental skills and punctuality through our collaborations, to Yona Baskharoun, for making uncountable phantoms, Haohan Xu, for the antenna measurements, to Sheng Tu for his enthusiasm and eternal happy face!

My friends bring the joy and peace to my life. I want to thank Yasmin, Leila, Mehdi and Stephan for being my family in Canada, for the warm and lovely thanksgiving and Christmas nights, for all the innocent delicious turkeys we had! I also would like to thank my dear friends, Kia and Pedram, for making life out of campus memorable and cheerful.

Last but not least I would like thank my family, for their unconditional love and support, my parents for their patient and encouragement, for helping me through all my life, my younger brother, Babak, whose wise comments makes him the actual elder one.

Kaveh Moussakhani, July 2014.

Contents

List of Figures

Chapter 1

Introduction

1.1 MOTIVATION

Microwave tissue imaging relies on the difference in the dielectric properties of the different tissues. For instance, the dielectric properties (permittivity and conductivity) of the malignant tissues in breast cancer are higher than those of normal breast tissue. This difference is referred to as dielectric contrast, which can be detected by microwave imaging (MWI) methods. MWI employs energy levels that do not harm the tissues. Its other advantage is that the equipment has lower cost than the currently widely used diagnostic tools, e. g., magnetic resonance imaging (MRI) or X-rays. Therefore, MWI has potential benefits in early-stage breast cancer detection respectively for screening of the population at risk.

MWI systems seek to address the limitations of today's standard imaging modalities for breast cancer detection. For instance, X-ray mammography may pose some health risk as it delivers ionizing radiation into the breast tissues. Other drawback of mammography is the pain associated with breast compression. It also has relatively low sensitivity especially in the case of radiologically dense breast tissue [1]. In the case of ultrasound, the images contain too many artifacts and ambiguities (such as shadowing, speckle, and non-quantified contrasts). These issues often result in insufficient effective resolutions, as well as a lack of specificity in distinguishing malignant and normal masses, as well as distinguishing between normal background tissue and suspected masses [1]. The main disadvantage of MRI is its operating cost. The long examination times and the use of a contrast agent (gadolinium) make it unsuitable for screening purposes. Also, access to this imaging tool is rather limited and may result in unacceptable delays in the time for testing [1].

To investigate the ability of MWI for breast cancer detection, several studies of the dielectric properties of biological tissues at microwave frequencies were carried out. The results show that the dielectric contrast between malignant and normal breast tissues is sufficient for early stage breast cancer detection [1]-[4].

Various acquisition setups have been considered for the microwave measurements of the breast [4]-[13]. These setups can be categorized into three groups: passive, active, and hybrid. In the passive systems, similar to radiometry, a sensor measures the radiated thermal electromagnetic energy. The energy detected by a radiometer at microwave frequencies is the thermal emission from the tissue itself as well as thermal emission from the environment that arrives at the radiometer after reflection. This intensity of emission is proportional to the temperature of tissue. Cancer detection relies on the fact that there is a temperature contrast between a malignant tumor and the surrounding normal tissue due to the difference in their metabolism [14].

In some systems, the contrast between malignant and normal tissue is increased further. To archive a better contrast, for example, microwave radiation can be used to induce heating. Such systems are examples of hybrid systems. For instance in microwave-induced acoustic imaging, microwaves are used to illuminate the breast. Due to the higher conductivity of malignant breast tissue, more energy is deposited in tumors, resulting in selective heating of these lesions. The tumors expand and generate pressure waves, which are detected by ultrasound transducers [15].

The active methods are based on the generation of microwave signals which are coupled into the tissue using antennas. The microwave signals penetrate into the tissue and are scattered. The scattered field can be also

extracted in three different scenarios; mono-static, bi-static or multi-static. In the mono-static scenario which is common in radar, the transmitting (Tx) and the receiving (Rx) antennas are co-located, and the waves are extracted at the point where they were generated. Moreover, to construct tissue images, scanning the Tx/Rx location over a sufficiently large surface (acquisition surface) is essential [16].

In a bi-static scenario, the Tx and Rx locations are different and one antenna transmits and only one antenna receives. To obtain tissue images similar to mono-static scenario either the Tx or the Rx antenna, or both, may be scanned over their respective surfaces [17]. A multi-static system is a generalization of the bi-static system, with one or more receivers extract microwave signals from one or more geographically separated transmitters. Scanning the Tx/Rx antennas may also be used in multi-static systems [18].

Most systems exploit active microwave imaging techniques. Here, also our focus is on active systems. The goals of microwave imaging design are increasing its capability to detect low-contrast and small-size tumors as well as reducing its size and cost. The improvement can be realized both in the hardware and the software system components. Here, the focus is on the hardware of the microwave imaging systems and the evaluation of its performance. As a matter of fact, the hardware of the microwave imaging

system has a primary role in determining the performance, the size and the cost of the system.

There are several challenges in MWI that need to be addressed in hardware design [19] [20]. One of these challenges is coupling microwave power into the tissue. Due to the large difference between the electrical properties of living tissue and air, the reflection of any microwave radiation generated in air at the tissue interface is significant. In general, different layers of tissue not only reflect back the microwave power but also limit its penetration through attenuation.

To reduce reflections and increase the coupling power into the tissue coupling liquids are used [21]. Although using coupling liquids reduces the reflections, it can still cause power loss due to spillovers and dissipation in the coupling liquid. Moreover, coupling liquids make the maintenance of the acquisition system more difficult in clinical implementations. Another approach to improve the power coupling into the tissue is to design the antennas so that they couple the power through direct contact with the tissue [22]. In this case, the acquisition system should be flexible for adjustments or deformations of setup to conform to the size and shape of the particular imaged tissue.

Low dynamic range of microwave imaging systems is another challenging factor. The loss in medium, sensor efficiency and uncertainty in tissue

measurements are major defining factors of dynamic range in microwave imaging systems. High dynamic range is desirable to achieve better microwave signal penetration depth and better sensitivity in the tumor detection.

In this thesis, we addressed some of the hardware design challenges. Moreover, several parameters describing the performance of the MWI systems are investigated. Methods to estimate the efficiency and the sensitivity of the MWI systems and their components have been introduced and applied in practical scenarios. These methods can be used to quantify the performance of MWI systems and to compare them.

1.2 DYNAMIC RANGE OF MICROWAVE IMAGING SYSTEMS

The dynamic range (DR or DNR) is the ratio between its largest and smallest possible values. It describes the range of the signal levels that can be reliably measured simultaneously; in particular, the ability to accurately measure small signals in the presence of the large signals [23]. The DR is an important parameter of any measurement system. In many applications such as spectral analysis, tomography, and communications, the DR should be as high as possible.

The maximum signal in the transmitter side is always limited in the acquisition system. In microwave tissue imaging, the maximum allowed transmitted power is limited by thermal effects due to the microwave radiation

absorbed in a living organism, which may cause tissue damage. The tissue damage depends primarily on the absorbed energy and the tissue thermal sensitivity. The absorbed energy is a function of the microwave power density (which depends on the distance from the source and its power output), the frequency, and the absorption rate in the given tissue. The effects of microwaves on tissues are well understood in principle but are still under investigation and characterization[23]. There are strict safety limits for the exposure of people to microwave radiation. The U.S. Occupational Safety and Health Administration defines the energy density limit for exposure periods of 0.1 hours or more to 10 mW/cm^2. For shorter periods, the limit is 1 $mW\text{-}hr/cm^2$ with limited excursions above 10 mW/cm^2 [24].

The microwave signal decays as it passes through the lossy tissue. Therefore, the signal level in the receiver side is controlled by the transmitter`s power and tissue loss. On the other hand, in the lower levels of the dynamic range, the small signal analysis is limited by two independent factors: the system noise floor and the spurious signals (any undesirable unpredictable signal that increases the uncertainty of the measurement). In this section, the noise floor of our imaging setup is investigated.

1.2.1 **Vector Network Analyzer Noise floor**

The dynamic range of the microwave imaging setup as a system is dictated by the dynamic range of its different parts. The noise level of a system sets the

lower limit of the magnitude of a signal that can be detected. The noise floor of the imaging system is determined by the noise floor of the measuring equipment. For *S*-parameter measurement, vector network analyzers (VNA) are used. In this section the noise performance of two VNAs, Advantest-R3770 and Agilent-E8363B, is investigated. The effect of the resolution bandwidth (RBW) and the averaging factor (AF) on the noise floor are measured and studied. The effect of a low noise amplifier on the noise floor is also examined.

1.2.2 **Noise Level of the Advantest VNA (R3770)**

The first step in measuring the noise level of the VNA is calibration. In order to see the performance of the instrument in its entire frequency range, the start and stop frequencies are set to 300 kHz and 20 GHz, respectively. Since $|S_{21}|$ represents the square root of the ratio of the received power to the transmitted power, by setting the output power of port one to 0 dBm, $|S_{21}|$ represents the actual noise level of the instrument in dBm. Then, other parameters like the RBW and the number of frequency points should be selected according to the experiment specifications.

When measuring the noise level, the receiving port is matched to a standard 50 Ω load. All other ports, including the transmitting port, are left open. A smoothing factor of 20% is used as suggested in the instrument manual for the case of noise measurement. The averaging is disabled. The averaging reduces

the noise level, so the highest noise level is measured with the averaging being off.

1.2.2.1 **The Effect of the Resolution Bandwidth on the Noise Level**

The thermal noise power is related to the measurement bandwidth Δf by [25]

$$P = k_B T \Delta f \tag{1.1}$$

where k_B is Boltzmann's constant and T is the absolute temperature. Therefore, the noise power is directly proportional to the RBW.

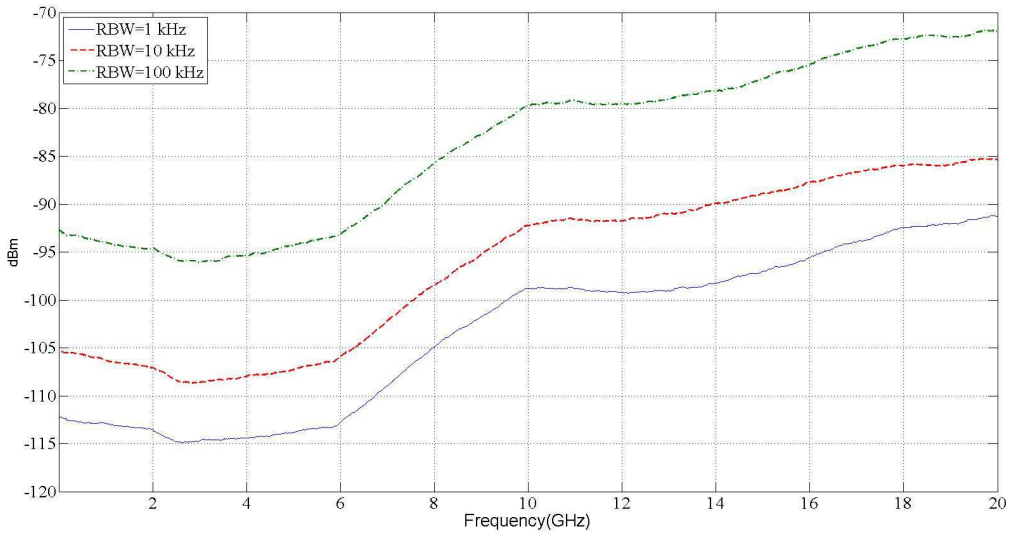

Fig. 1.2-1. Noise level of the Advantest VNA for different RBWs (smoothing = 20%, AF = 0, transmitter power = 0 dBm, number of frequency points = 1601).

Fig. 1.2-1 shows the noise level of this instrument for different RBW values. The noise performance of this VNA is not flat in its entire frequency

range. The differences in the noise levels for a given RBW are due to the different receivers used in the different frequency ranges.

Since the noise level decreases by the decreasing the RBW, one may desire the smallest RBW. On the other hand, the measurement time depends on the RBW. For a lower RBW, the measurement lasts longer. The sweep times for several RBW values are summarized in Table 1.2-1.

Table 1.2-1. Sweep time for different resolution bandwidths with 1601 frequency points.

RBW (kHz)	Sweep time (s)
1	1.486
5	0.397
10	0.195
100	0.042

1.2.2.2 **The Effect of Averaging on the Noise Level**

As noise is a random phenomenon, averaging the measured signal decreases the noise level of the VNA. Fig. 1.2-2 shows the effect of the averaging factor (AF) on the noise level of the Advantest VNA. Increasing the AF decreases the noise level and increases the measurement time.

The measurement time (MT) of the VNA can be related to the AF and the sweep time (ST). To find the relationship, several measurements were carried out for different MT, AF and ST. Our calculations show that, for the Advantest VNA, this relationship is linear and can be expressed as

$$MT \approx 2(AF+1)ST\,. \tag{1.2}$$

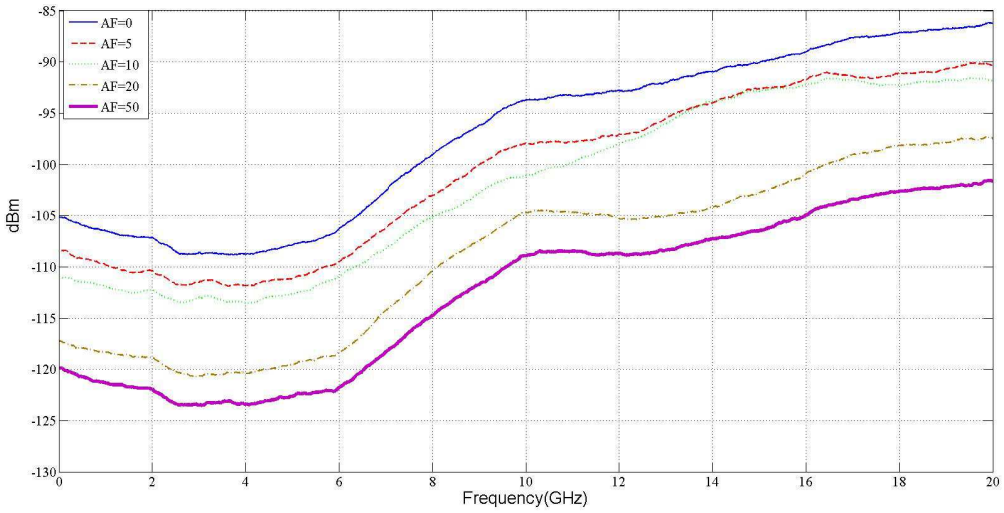

Fig. 1.2-2. Effect of averaging on the noise level of the Advantest VNA (smoothing = 20%, RBW = 10 kHz, transmitter power = 0 dBm, number of points = 1601).

The factor of 2 in (1.2) is due to the post-processing time of the VNA. As it can be seen in Fig. 1.2-1 and Fig. 1.2-2, the RBW and the AF have significant effects on the measured noise level of the VNA. They also affect the measurement time. Therefore, selecting these factors is a trade-off between noise level and measurement time.

1.2.3 **NOISE LEVEL OF THE AGILENT VNA (E8363B)**

The same parameter settings as those in the Advantest VNA measurements are used in the Agilent VNA measurements. This VNA has restrictions on the choice of some of these parameters. By selecting the highest frequency at 40 GHz (the maximum frequency in the range of this instrument), the RBW can be between 1 kHz and 40 kHz.

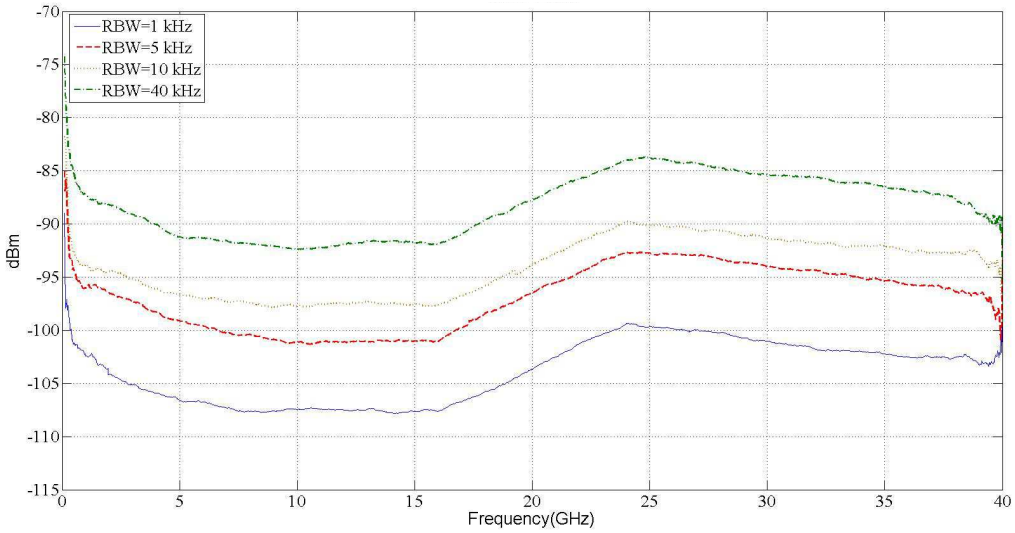

Fig. 1.2-3. Noise level of the Agilent VNA for different RBW (smoothing = 20.42%, AF = 0, transmitter power = 0 dBm, number of point = 1601).

1.2.3.1 **Resolution Bandwidth Effect on the Noise Level**

The noise levels for the different RBW values are shown in Fig. 1.2-3. The effect of the RBW is similar to that in the measurements with the Advantest VNA

1.2.3.2 **The Effect of Averaging on the Noise Level**

Similar to the Advantest VNA, increasing the AF decreases the noise level of the Agilent VNA; see Fig. 1.2-4. The observed measurement time with the Agilent VNA is half that of the Advantest VNA:

$$MT \approx (AF + 1)ST \,. \tag{1.3}$$

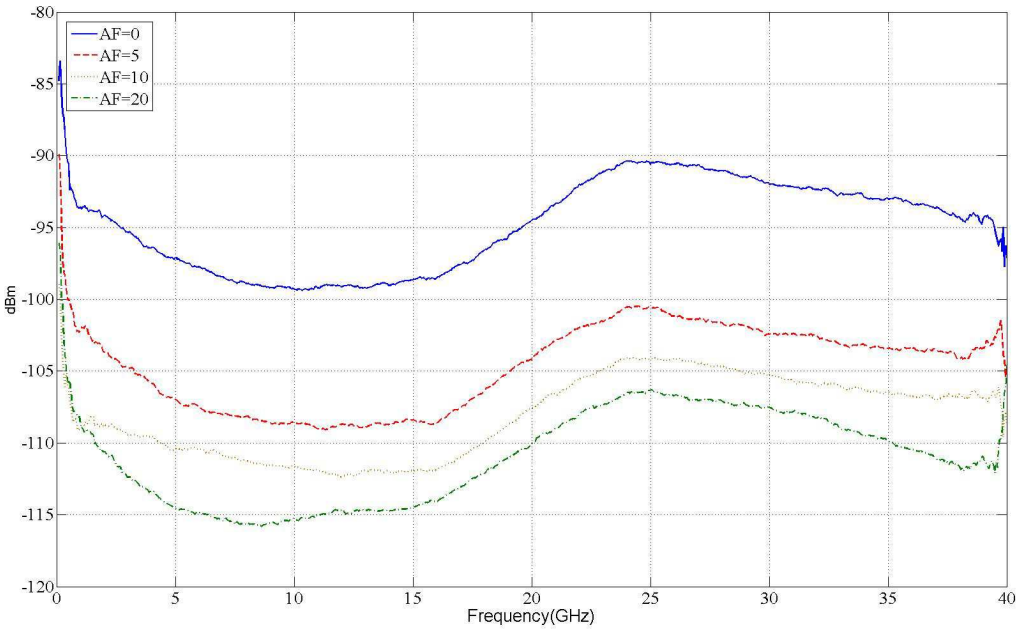

Fig. 1.2-4. Effect of averaging on noise level of the Agilent VNA (smoothing = 20.42%, RBW = 10 kHz, transmitter power = -1 dBm, number of points = 1601).

1.2.4 **NOISE LEVEL COMPARISON**

The noise levels of the two instruments in the desired frequency range (from 3 GHz to 10 GHz) are shown in Fig. 1.2-5 for set values of RBW and the AF. As seen from the figure, the noise level for the Advantest VNA is smaller than

that of the Agilent VNA in the frequency range from 3 to 7.5 GHz, and it becomes higher for frequencies above 7.5 GHz.

1.2.5 NOISE LEVEL WITH LOW-NOISE AMPLIFIERS

An ideal amplifier would have no noise of its own, but would simply amplify its input (the signal and the noise). Therefore, the noise floor at the output of the amplifier is higher than that at the input by a factor equal to its gain. The ideal noiseless amplifier does not change the signal-to-noise ratio (SNR). But a real amplifier not only amplifies the noise at its input, but will contribute its own noise to signal, as shown in Fig. 1.2-6. and (1.4).

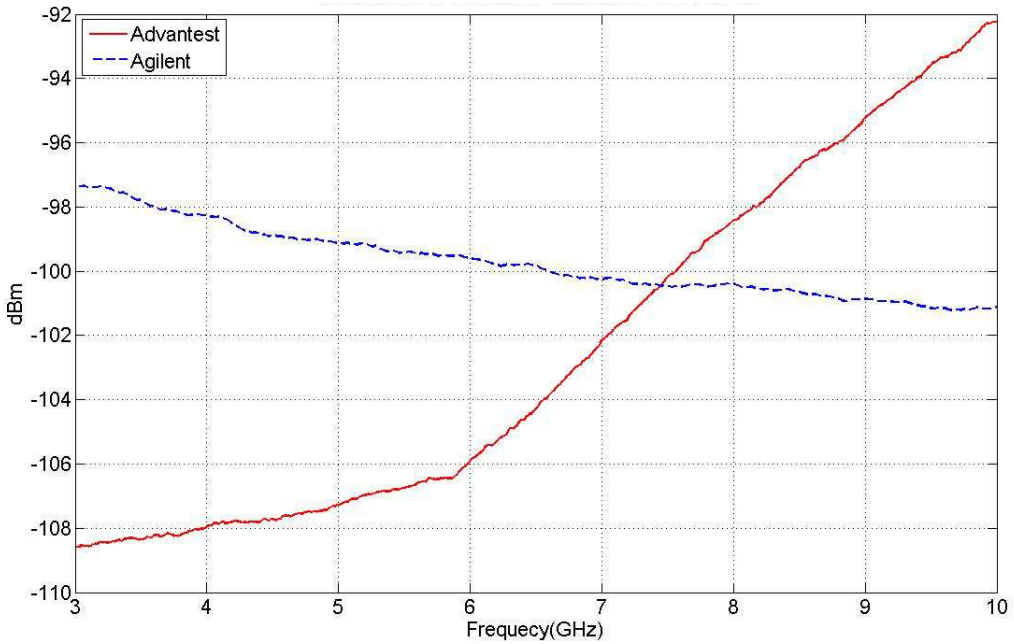

Fig. 1.2-5. Noise levels of the Advantest and the Agilent VNAs (smoothing = 20%, RBW = 10 kHz, AF = 0, transmitter power = 0 dBm, number of points = 1601).

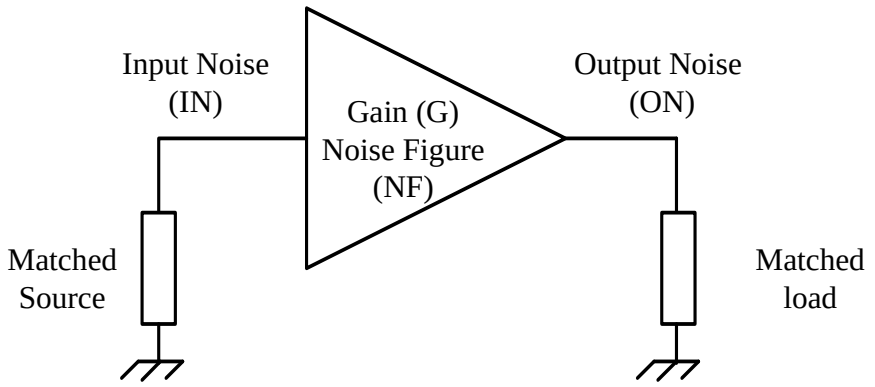

Fig. 1.2-6. Schematic of an amplifier and its parameters

$$ON\ (dB) = IN\ (dB) + G\ (dB) + NF\ (dB) \tag{1.4}$$

In which IN is the noise at the input and ON is the noise at the output of the amplifier. G is the gain of amplifier, and NF is the noise figure of the amplifier.

This reduces the SNR at the output of the amplifier and consequently the dynamic range of the whole system. The real amplifier has two major internal components: an ideal noiseless amplifier and a noise source. The noise source adds noise to any signal that enters the amplifier. Then the ideal amplifier amplifies both the signal and aggregate noise by an amount equal to its gain.

Even though an amplifier reduces the SNR at the input of the VNA receiving port, it can be in fact increase the dynamic of the MWI system. If the noise in the measurement environment is lower than the noise floor of the VNA, the low-noise amplifier will increase the dynamic range. In the

following section, the effect of a low-noise amplifier on the noise floor and the dynamic range of the system is explored.

1.2.5.1 **Effect of Cascade Amplifiers on the Dynamic Range**

The contribution of the amplifier's noise source is fixed and does not change with the input signal. Therefore, when more noise is present at the amplifier input, the contribution of the internal noise source is less significant in comparison. When amplifiers are cascaded together in order to amplify very weak signals, it is the first amplifier in the chain, which has the greatest influence upon the SNR because the noise floor is the lowest at that point in the chain. This can be expected bearing in mind the Friss equation [26]:

$$T_{\text{eq}} = T_1 + \frac{T_2}{G_1} + \frac{T_3}{G_1 G_2} + \ldots . \tag{1.5}$$

Here, T_{eq} is the resulting noise temperature referred to the input, T_1, T_2 and T_3 are the noise temperatures of the first, second and third stage in the cascade, respectively; G_1 and G_2 are the power gains of the first and the second stage in the cascade, respectively.

As the first amplifier in a cascade has the most significant effect on the total noise figure, amplifier with the lowest noise figure should be first (assuming all else is equal). This also applies to the gain. If two amplifiers

have the same noise figure but different gains, the higher gain amplifier should precede the lower gain amplifier.

In our experiments, two cascade low-noise amplifiers are connected to the receiver port (port 2) of the VNA. Port 1 the transmitting port is loaded with a standard 50-Ω load. The amplifiers are similar and each of them has 26 dB gain and 3 dB noise figure. The result is shown in Fig. 1.2-7. The jump in the noise level of the VNA approximately (35 dB), is less than the summation of the gains of the two amplifiers and the resulting noise temperature approximately (55dB). This translates into an increase of dynamic range by 20 dB. Therefore, if the noise in the measurement environment is lower than the noise floor of the VNA, low noise amplifiers can be used to increase the dynamic range of the MWI system.

We investigated the noise floor of two vector network analyzers to find the lowest limit of the dynamic range of our microwave imaging setup. The smaller noise level corresponds to smaller RBW and larger averaging factor. However, both small RBW and large averaging factor, prolong the measurement time. A tradeoff should be made between noise level and measurement time.

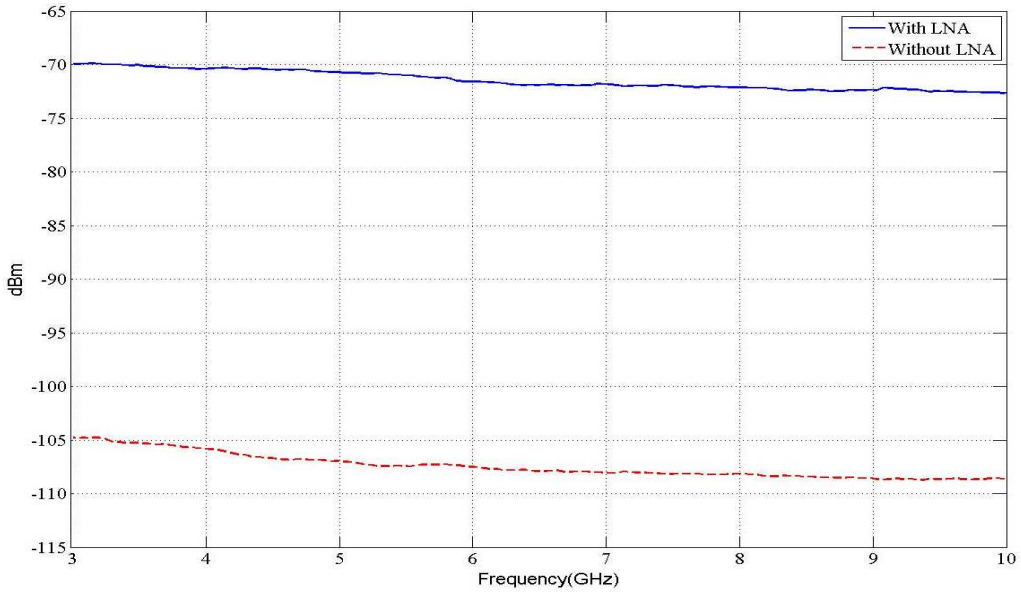

Fig. 1.2-7. Effect on the noise level of a connecting two-stage LNA at the receiving side of Agilent VNA (smoothing = 20%, RBW = 10 kHz, AF = 5, transmitter power = 0 dBm, number of frequency points = 1601).

The effect of low-noise amplifiers on the noise floor is also investigated. The use of low noise amplifiers can only be useful in increasing the dynamic range when the noise level of the measurement environment is lower than the VNA noise floor (at least as much as the noise figure of the amplifier). If a cascade of amplifiers is going to be used in the receiver side, the lower noise figure and higher gain amplifier should be first in a line of amplifiers to achieve the best overall noise figure.

We focused on the dynamic range of the VNA as the largest achievable dynamic range of a MWI setup. There are several other factors, which can

introduce noise and uncertainty into the MWI system and decrease its dynamic range. Beside the noise figure of amplifiers, the noise figures of antennas are also important. The tissue itself has a noise figure. The leakage or any electromagnetic interference will also increase the noise floor of the measurement setup. Moreover, any mechanical movement can introduce measurement uncertainty, which in effect acts like noise to the measurement. Some of these effects were explored in [28]. In Chapter 4 the importance of the noise and the measurement uncertainty for the sensitivity of the MWI system will be further investigated. In the next Chapter, we introduce a new high-efficiency antenna, which increases the dynamic range of the microwave MWI imaging system.

1.3 OUTLINE OF THE THESIS

Chapter 2 introduces a new high efficiency ultra wide band TEM horn antenna for breast cancer detection. The efficiency of the antenna is one of the important parameters, in its design. It affects the dynamic range of the whole imaging setup. Beside high efficiency, the new antenna also has several advantages other over pervious designs. The need for coupling liquids is eliminated by enclosing the radiating structure in a solid dielectric medium. This simplifies the acquisition setup. It also increases the overall coupling efficiency of the system by increasing the power coupled into the tissue.

Moreover, the new antenna blocks the electromagnetic interference from the surrounding medium by being fully shielded (except the front aperture which comes in contact with the tissue). The leakage in the surrounding medium (air) is eliminated thus reducing the parasitic coupling between the transmitting and receiving antennas to a minimum.

In Chapter 3 a measurement-based method to evaluate the efficiency of antennas used in microwave tissue imaging is proposed. The method is versatile and in principle applicable to antennas operating in free space as well. Two identical antennas are employed, one transmitting and the other one receiving. A signal flow graph (SFG) is developed for the two-port network formed by the antennas and the medium between them. The medium's electrical properties mimic those of tissue and can vary according to the application. Several measurements are performed with one of the antennas being loaded with known loads. A system of equations is constructed from the acquired data. The solution of this system produces the efficiency of the antenna in addition to other unknown parameters of the SFG. The efficiencies of two antenna designs are estimated from measured and simulated data and are verified through comparisons.

Chapter 4 introduces a new performance metric for MWI systems, namely, the physical contrast sensitivity. Methodologies are proposed for its evaluation through measurements and through simulations. This enables the estimation of

the smallest detectable target permittivity contrast or size for the system under evaluation. The outcomes of the proposed simulation-based and measurement-based methods are compared for the case of a realistic tissue-imaging system. The agreement between the simulated and measured sensitivity estimates validates the proposed methods. The intention of the proposed methodology is to provide common means to quantify and compare the sensitivity performance of microwave systems used in tissue imaging as well as the antennas used as sensors. The proposed method targets the performance of the hardware and it is not concerned with the image-reconstruction algorithms.

The thesis concludes with Chapter 5 where conclusions and recommendations for the future work are given.

1.4 CONTRIBUTIONS

The author has contributed to a number of original developments presented in this thesis. These are briefly described next.

(1) A new high efficiency ultra wide band TEM horn antenna for breast cancer detection is introduced [29][30][31].

(2) A measurement-based method to evaluate the efficiency of antennas used in microwave tissue imaging is proposed [32][33].

(3) The physical contrast sensitivity of microwave imaging systems employing scattering-parameter measurements is introduced. This

provides common means to quantify and compare the sensitivity performance of microwave systems used in tissue imaging as well as the antennas used as sensors [34][35].

1.5 REFERENCES

[1] "Screening for breast cancer: U.S. preventive services task force recommendation statement," *Annals of Internal Medicine*, vol. 151, no. 10, pp. 716–737, Nov. 2009.

[2] S. Poplack, T. Tosteson, W. Wells, B. Pogue, P. Meaney, A. Hartov, C. Kogel, S. Soho, J. Gibson, and K. Paulsen, "Electromagnetic breast imaging: Results of a pilot studying women with abnormal mammograms," *Radiology*, vol. 243, no. 2, pp. 350–359, May 2007.

[3] L. Sha, E. Ward, and B. Stroy, "A review of dielectric properties of normal and malignant breast tissue," in *Proc. IEEE Southeast Conf*, 2002, pp. 457–462.

[4] P. Meaney, M. Manning, D. Li, S. Poplack, and K. Paulsen, "A clinical prototype for active microwave imaging of the breast," *IEEE Trans. Microw. Theory Techn.* vol. 48, pp. 1841-1853, Nov. 2000.

[5] P. M. Meaney, A. P. Gregory, N. R. Epslein, and K. D. Paulsen, "Microwave open-ended coaxial dielectric probe: interpretation of the

sensing volume revised," *BMC Medical Physics*, vol. 14, no. 3, Jun. 2014.

[6] A. Rosen, M. Stuchly, and A. V. Vorst, "Applications of RF/Microwaves in medicine," *IEEE Trans. Microw. Theory Techn*. vol. 50, no. 3, pp. 963–974, Mar. 2002.

[7] X.Li, S. Davis, S. Hagness, D. van der Weide, and B. V. Veen, "Microwave imaging via space-time beamforming: Experimental investigation of tumor detection in multilayer breast phantoms," *IEEE Trans. Microw. Theory Techn.* vol. 52, no. 8, pp. 1856–1865, Aug. 2004.

[8] X.Li, E. Bond, B. V. Veen, and S. Hagness, "An overview of ultra-wideband microwave imaging via space-time beamforming for early-stage breast-cancer detection," *IEEE Antennas and Propag. Mag.* vol. 47, no. 1, pp. 19–34, Feb. 2005.

[9] E. Bond, X. Li, S. Hagness, and B. V. Veen, "Microwave imaging via space-time beamforming for early detection of breast cancer," *IEEE Trans. Antennas and Propag*. vol. 51, no. 8, pp. 1690–1705, Aug. 2003.

[10] J. Bourqui, M. Campbell, J. Sill, M. Shenouda, and E. Fear, "Antenna performance for ultra-wideband microwave imaging," *IEEE Radio and Wireless Symposium (RWS 2009)*, pp. 522–525, Jan. 2009.

[11] E. Fear and M. Stuchly, “Microwave detection of breast cancer,” *IEEE Trans. Microw. Theory. Techn.* vol. 48, no. 11, pp. 1854–1863, Nov. 2000.

[12] E. Fear, S. Hagness, P. Meaney, M. Okoniewski, and M. Stuchly, “Enhancing breast tumor detection with near-field imaging,” *IEEE Microw. Mag.* pp. 48–56, Mar. 2002.

[13] E. Fear, X. Li, S. Hagness, and M. Stuchly, “Confocal microwave imaging for breast cancer detection: Localization of tumors in three dimensions,” *IEEE Trans. Biomed. Eng.* vol. 49, no. 8, pp. 812–822, Aug. 2002.

[14] A. H. Barrett and P. C. Myers. *Basic Principles and Applications of Microwave Thermography. In Medical Applications of Microwave Imaging*, Larsen, L. E., and Jacobi, J. H., Eds.; IEEE Press: New York, 1986.

[15] L. V. Wang, X. Zhao, H. Sun, and G. Ku. “Microwave-induced acoustic imaging of biological tissues.” *Review of Scientific Instruments* vol. 70, no. 9, pp. 3744-3748, Mar. 1999.

[16] E. Fear, J. Bourqui, , C. Curtis, D. Mew, , B. Docktor, , and C. Romano, “Microwave breast imaging with a monostatic radar-based system: a study of application to patients,” *IEEE Trans. Microw. Theory Techn*, volume 61, issue 5, pp. 2119-2128, May 2013.

[17] Y. Zhang, S. Tu, R.K. Amineh, and N.K. Nikolova, “Sensitivity-based microwave imaging with raster scanning,” *IEEE MTT-S Int. Microwave Symp*., pp. 1-3, 2012.

[18] Klemm, Maciej, Ian J. Craddock, Jack A. Leendertz, Alan Preece, and Ralph Benjamin. “Radar-based breast cancer detection using a hemispherical antenna array—experimental results.” *IEEE Trans. Antennas Propag*, vol. 57, no. 6 pp. 1692-1704, Jun 2009.

[19] N.K. Nikolova, “Microwave biomedical imaging,” *Wiley Encyclopedia of Electrical and Electronics Engineering*, pp. 1–22. (published on-line Apr. 25, 2014)

[20] N.K. Nikolova, “Microwave near-field imaging of human tissue and its applications to breast cancer detection,” *IEEE Microw. Mag*., vol. 12, no. 7, pp. 78–94, Dec. 2011.

[21] P. M. Meaney, M. W. Fanning, T. Raynolds, C. J. Fox, Q. Fang, S. P. Poplack, and K. D. Paulsen, “Initial clinical experience with microwave breast imaging in women with normal mammography,” *Academic Radiology*, vol. 14, pp. 207–218, Feb. 2007.

[22] R. K. Amineh, M. Ravan, A. Trehan, and N. K. Nikolova, “Near-field microwave imaging based on aperture raster scanning with TEM horn antennas” *IEEE Trans. Antennas Propag.*, vol. 59, no. 3, pp. 928–940, Mar. 2011.

[23] J. Halamek, I. Viscor, and M. Kasal, “Dynamic range and acquisition system,” *Measurement Science Review* 1, no. 1, pp. 71–74, 2001.

[24] P.S. Yarmolenko *et. al*. “Thresholds for thermal damage to normal tissues: An update” *Int. J. Hyperthermia*, vol. 27, no.4, pp. 320–343, June 2011.

[25] R. L. Brauer, *Safety and Health for Engineers.* John Wiley, New Jersey, Hoboken, 2006.

[26] K. McClaning and T. Vito, *Radio Receiver Design*: Noble Publishing Corporation, Atlanta, GA, 2000.

[27] H. T. Friss,“Noise figure of radio receiver,” *Proceedings of the IRE,* vol. 32, no. 7, pp.419–422, 1944.

[28] *Agilent: Fundamentals of RF and microwave noise figure measurements*, Application Note 57-1, Agilent Technologies, [Online].

[29] H. Xu, Planar *Raster-scanning System for Near-field Microwave Imaging*. M.A.Sc. Thesis, McMaster University, 2011.

[30] K. Moussakhani, R.K. Amineh, and N.K. Nikolova, “High-efficiency TEM horn antenna for ultra-wide band microwave tissue imaging,” *IEEE AP-S/URSI Int. Symp. on Antennas and Propagation*, July 2011.

[31] R. K. Amineh, K. Moussakhani, Li Liu, H. Xu, M. S. Dadash, Y. Baskharoun, and N. K. Nikolova, “Practical issues in microwave raster

scanning," European Conf. on Antennas and Propagation (EuCAP) 2011, April 2011.

[32] K. Moussakhani, R.K. Amineh, and N.K. Nikolova, "Estimating the efficiency of antennas used as sensors in microwave tissue measurements," *IEEE Trans. Antennas Propag*. vol. 62, no. 1, pp. 295-301, Jan. 2014.

[33] K. Moussakhani, R.K. Amineh, and N.K. Nikolova, "Evaluating the efficiency of antennas used as sensors in microwave tissue measurements," *IEEE AP-S/URSI Int. Symp. on Antennas and Propagation*, July 2013.

[34] K. Moussakhani, J. McCombe, and N.K. Nikolova, "Sensitivity of microwave imaging systems employing scattering-parameter measurements," IEEE Trans. Microw. Theory .Techn. (*in press*).

[35] K. Moussakhani, J. McCombe, and N.K. Nikolova, "Sensitivity of microwave imaging systems employing scattering-parameter measurements," *IEEE AP-S/URSI Int. Symp. on Antennas and Propagation*, July 2014.

Chapter 2

Antenna Design for Microwave Imaging

2.1 INTRODUCTION

The antenna is an important part of a microwave imaging setup. In tissue imaging, it needs to satisfy several requirements. In some microwave imaging applications, the typical design requirements, which have been considered in previous designs, are wide impedance bandwidth, high directivity, good efficiency, and small size. Different kinds of antennas have been introduced for near-field microwave imaging such as the planar monopole [1], the slot antenna [2], the Fourtear antenna [3], the microstrip patch antenna [4], the planar “dark-eyes” antenna [5], a cross-Vivaldi antenna [6], a ridged pyramidal horn [7], and a TEM horn [8].

2.2 NEW UWB ANTENNA FOR MICROWAVE IMAGING

The efficiency of the antenna is one of its important design parameters. It affects the dynamic range of the whole microwave imaging setup. In this chapter, a new ultra-wide band high efficiency TEM horn antenna is presented. Beside its high efficiency, the new antenna also has several advantages over pervious designs. Similarly to the TEM horn in [8], the need for coupling liquids is eliminated by enclosing the radiating structure in a solid dielectric medium. The elimination of the coupling liquid significantly simplifies the acquisition setup and its maintenance. It also increases the efficiency of the system by improving the coupling power. Unlike the antenna in [8], the new antenna blocks the electromagnetic interference from the surrounding medium by being fully shielded (except the front aperture which comes into contact with the tissue phantom). The leakage in the surrounding medium (air) is eliminated, thus reducing the parasitic coupling between the transmitting and receiving sensors to a minimum. Thus, with the new antenna design, the dynamic range of the imaging system is increased due to: 1) increase in the efficiency of the sensor, and 2) suppressing the spurious signals.

The ultra-wide band (UWB) performance of the antenna is verified through simulation and measurement. Excellent coupling efficiency is also demonstrated through simulation results.

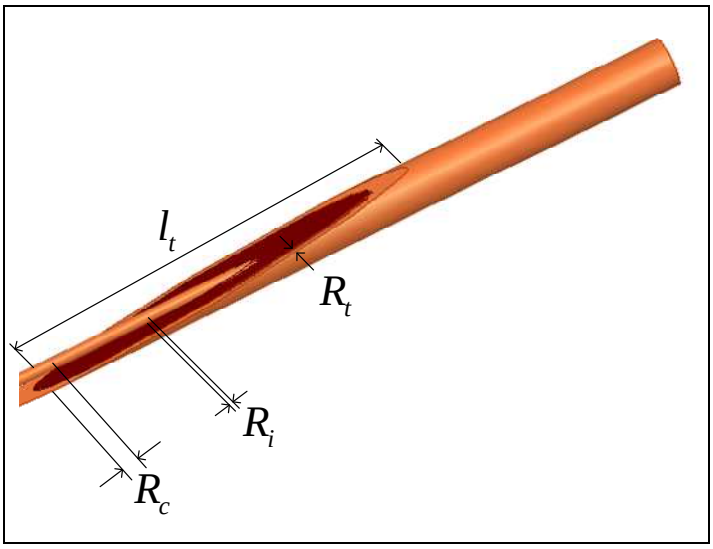

Fig.2.2-1. Tapered balun transformer.

2.2.1 **New Antenna Design**

The UWB TEM horn antenna is matched to a 50 Ω coaxial cable through a balun. The balun provides good impedance match in a UWB (from 3 GHz to 10 GHz). It transitions form the unbalanced coaxial cable to the balanced TEM line, which leads to the TEM horn.

A wide-band coaxial balun between a coaxial line and a twin-lead line has been introduced in [9]. Another similar wide-band balun from a coaxial line to a parallel-plate line has been proposed in [10]. These baluns are based on the gradual angular removal of the outer conductor of the coaxial line. In [11], the balun was used in a TEM horn design for the generation of high-power subsecond pulses. Similarly to [9] and [10], here a balun is used as a transition from the unbalanced coaxial line to the balanced TEM horn plates as shown in

Fig.2.2-1. As the figure shows, the outer conductor and the dielectric of the coaxial line are tapered toward the TEM horn plates. Theoretically, the balun has no upper frequency limit other than the frequency where higher order coaxial modes are supported [9].

The balun is connected to two flared metallic plates that to form the TEM horn antenna. The TEM horn is placed in a solid dielectric medium with $\varepsilon_r = 10$ and $\tan\delta = 0.01$ as shown in Fig. 2.2-2(a). The permittivity of 10 is the weighted averaged tissue permittivity of a breast in the UWB frequency range [12]. This permittivity value ensures maximum coupling of the microwave power into the tissue.

In addition, the whole structure is shielded from the outside environment (except the front aperture) as shown in Fig. 2.2-2(b). This ensures good isolation and minimal electromagnetic interference from the surrounding medium. It also reduces sideway leakage along the tissue-air interface.

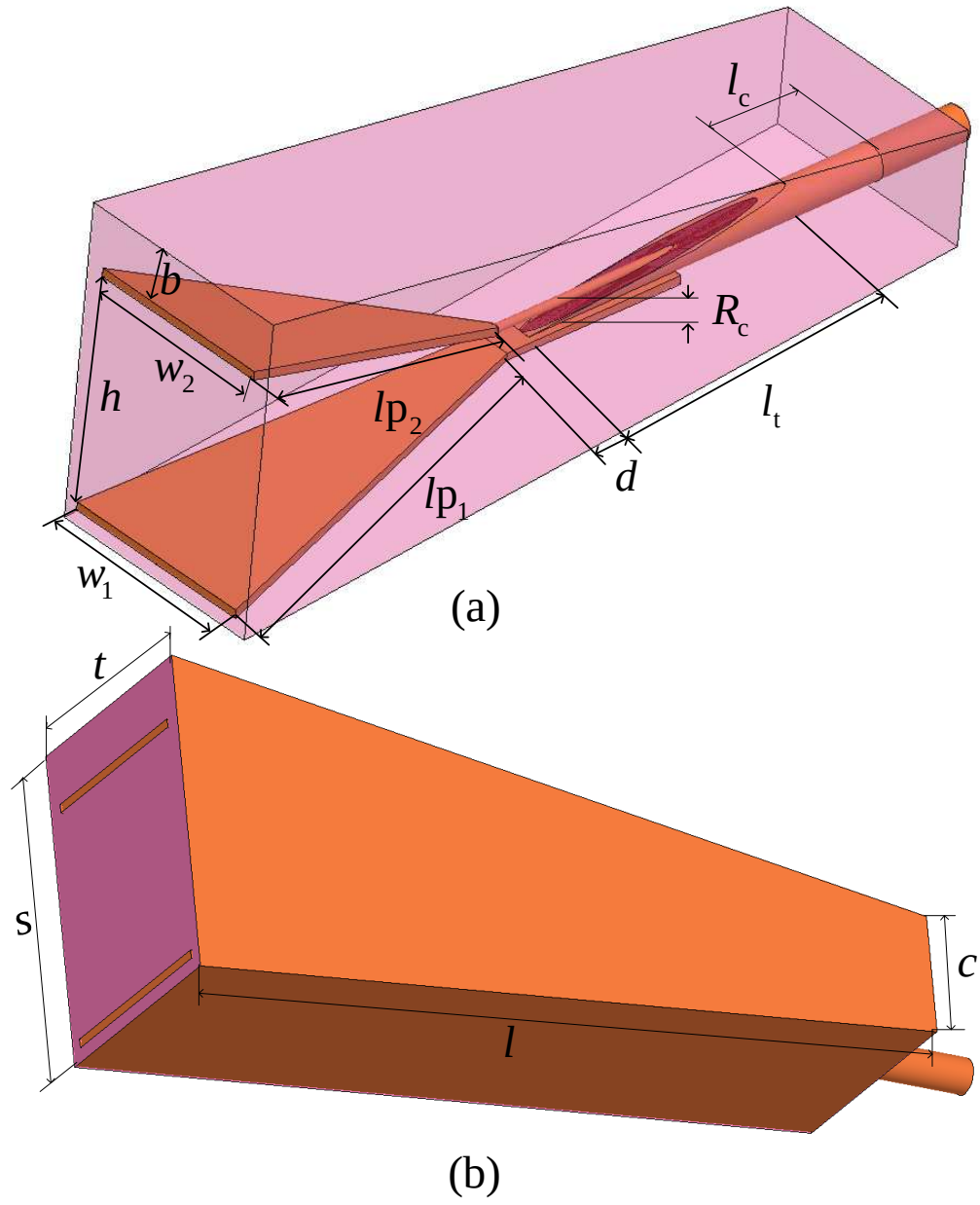

Fig. 2.2-2. TEM horn structure (a) TEM horn inside the solid dielectric medium with $\varepsilon_r = 10$ and $\tan\delta = 0.01$. (b) Shielded TEM horn.

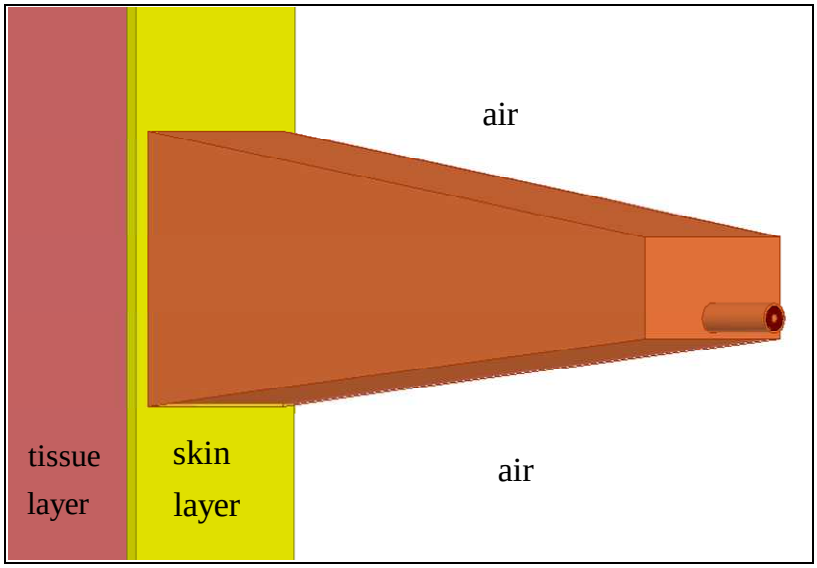

Fig. 2.2-3. Simulation configuration of TEM horn antenna.

The most important design shape parameters for this antenna are the balun's length l_t, widths w_1,w_2 and the lengths l_{p1}, l_{p2} of the TEM horn plates, the maximum distance between the horn plates h, and the dimensions of the soild dielectric block (c, s, t, l); see Fig. 2.2-2. These parameters have been optimized using an optimizer based on the self-adjoint sensitivity analysis tool in Ansoft's HFSS ver. 12 [13].

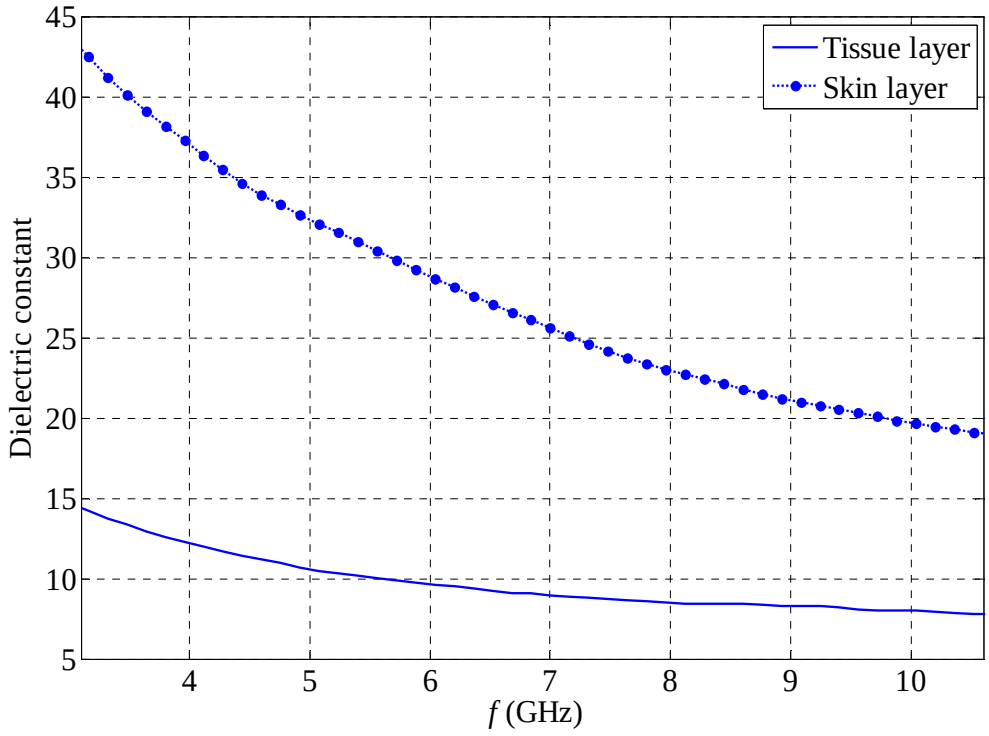

Fig. 2.2-4. Measured dielectric constant of the phantom`s tissue and skin layers made using glycerin-based recipies.

Fig. 2.2-3 shows the simulation configuration in HFSS, in which the antenna operates with its front aperture attached to two layers: a skin layer and a tissue layer. The dielectric properties of the breast tissues reported in [15] have been considered when making the tissue phantoms. The dielectric properties of these tissue phantoms are measured with the Agilent 85070E Performance Dielectric Probe Kit [16]. Fig. 2.2-5 and Fig. 2.2-5 show the measured relative permittivity and effective conductivity of the phantoms.

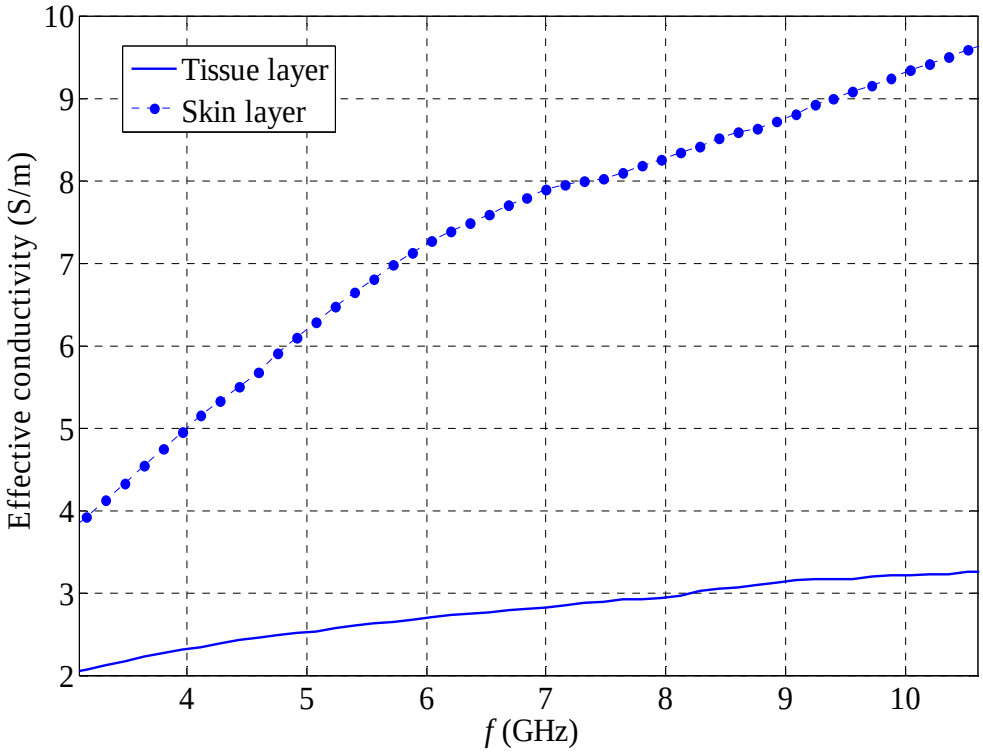

Fig. 2.2-5. Measured effective conductivity of the phantom`s tissue and skin layers made using glycerin-based recepies.

These phantom properties are also used in the simulation. The antenna parameters have been optimized so that the antenna is matched to a 50 Ω coaxial cable in the whole UWB frequency range.

2.2.2 **Antenna performance**

Table 2.2-1 shows the optimized design parameters of the proposed TEM horn. The total length of the antenna is 81.6 mm and the aperture size is 22 mm × 32 mm.

A prototype of the antenna is fabricated. Most parts of the solid dielectric block are machined out of ECCOSTOCK® HiK cement from Emerson & Cuming Microwave Products [17], the properties of which are $\varepsilon_r = 10$ and $\tan\delta < 0.002$ in the frequency range from 1 GHz to 10 GHz. Copper sheets are attached to the relevant parts of the antenna and then all pieces are attached together. Finally, the remaining dielectric parts are made out of dielectric cement material ECCOSTOCK® HiK Cement from Emerson & Cuming Microwave Products [17] ($\varepsilon_r = 10$ and $\tan\delta$ < 0.01 in the frequency range from 1 GHz to 10 GHz).

Table 2.2-1. Design parameters of the TEM horn antenna.

Parameter	Value (mm)	Parameter	Value (mm)
l_t	33	w_2	19.2
R_t	0.35	b	5.7
R_c	1.78	h	23.4
R_i	0.43	l_c	10
d	3	c	12

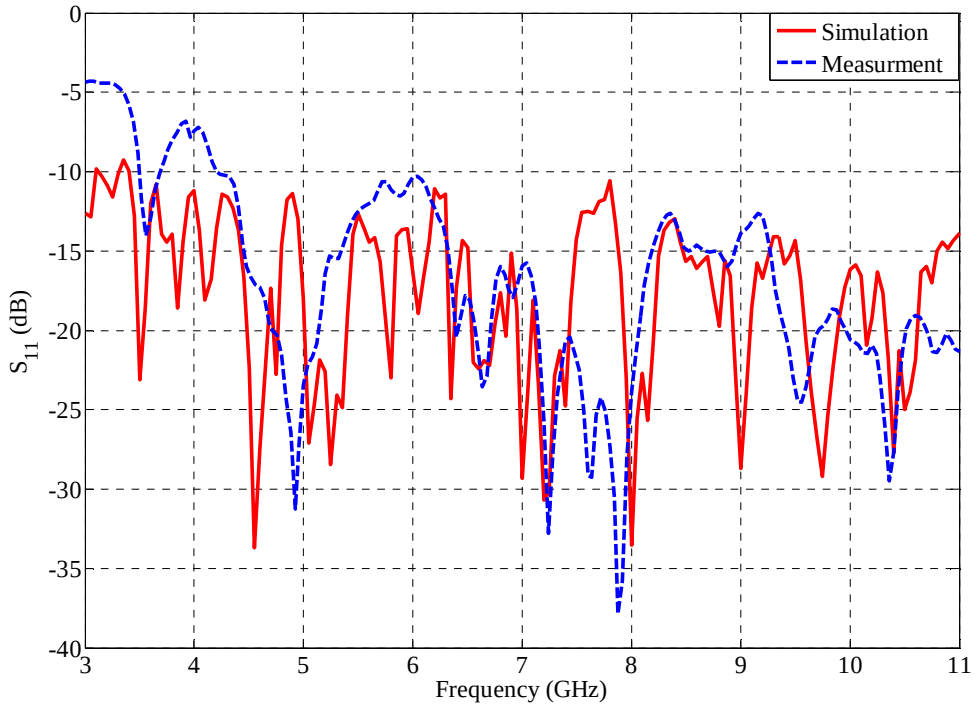

Fig.2.2-6. Measured and simulated reflection coefficient of the antenna.

To test the antenna performance, two glycerin-based phantom layers are made emulating the skin and the tissue with properties as those shown in Fig. 2.2-5 and Fig. 2.2-5. Fig.2.2-6 compares the measured reflection coefficient of the antenna with the simulated one. It is evident that, the antenna features good impedance match within the UWB. The observed resonances in the $|S_{11}|$ response are largely due to the reflections from the skin interface (or the end of the horn) as well as the intrinsic resonances of the shielding. In fact, these resonances are crucial in achieving the impedance match in the whole UWB. Since the proposed antenna has a more complicated structure than a TEM horn

in open space, many resonances can be expected, which depend on the dimensions and the constitutive parameters of the dielectric medium, the shielding, and the balun.

The other investigated parameter is the coupling efficiency computed as

$$e_c = \frac{P_c}{P_{in}}. \tag{2.1}$$

P_c and P_{in} are the power coupled into the tissue and the input power, respectively. P_c is computed in the simulations as the flux integral of the real part of the Poynting vector over the antenna aperture. Fig. 2.2-7 shows the variation of e_c versus frequency over the UWB for the proposed antenna and for the antenna in [8]. This figure shows a significant improvement in the coupling efficiency for the proposed antenna. The average coupling efficiencies over the UWB for the proposed antenna and the antenna in [8] are 0.87 and 0.37, respectively. The main reason for this improvement is the complete shielding of the antenna as compared to the partial shielding of the antenna in [8].

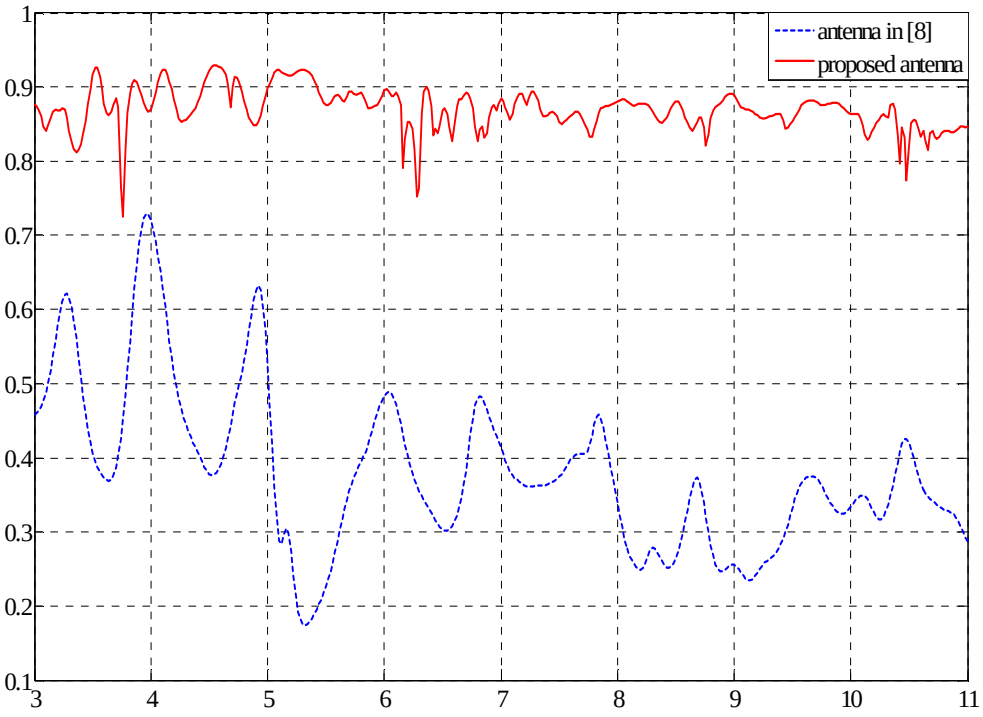

Fig. 2.2-7. Comparison of the coupling efficiencies of the proposed antenna and the antenna in [8].

In order to study the improvement in the performance of the imaging system based on the measurement of transmission coefficients, we simulate the transmission coefficient when two antennas are placed face-to-face on opposite sides of a compressed tissue phantom. This investigation is performed for both the proposed antenna and the antenna in [8]. Fig.2.2-8 shows the respective setup. The tissue thickness is 5 cm with two layers of skin placed on both sides with thicknesses of 1.5 mm. The same setup is used for the antenna in [8].

Fig. 2.2-9 shows the comparison of the transmission coefficients for the setup with the proposed antenna and the setup with the antenna in [8]. Overall, the transmission coefficient for the proposed antenna is larger than the transmission coefficient computed for the same setup with the antenna in [8]. An average of −96 dB for the transmission coefficient is computed for the proposed antenna over the UWB compared to an average of −102 dB for the antenna in [8]. This already shows that the transmission coefficient is increased by an average factor of 2 (6 dB) when using the proposed antenna. This improvement is due to the significant increase in the coupling efficiency

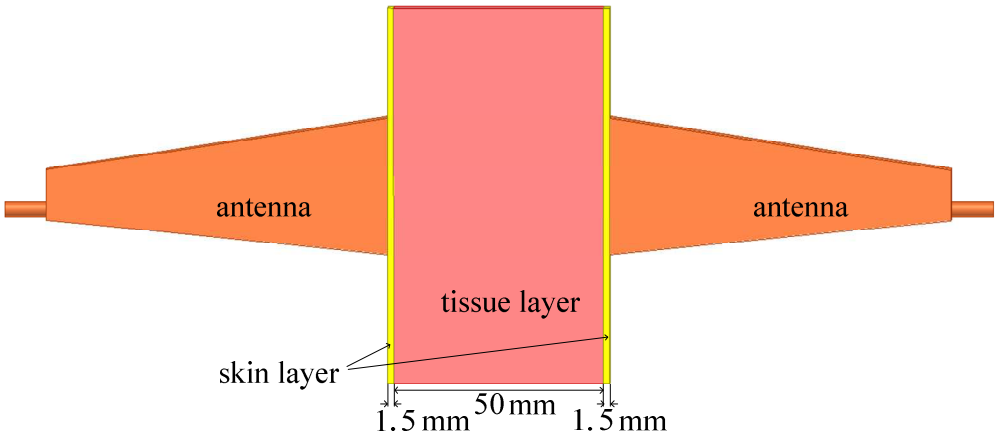

Fig.2.2-8. Setup for simulation of the transmission coefficient between two antennas placed on opposite sides of a compressed tissue.

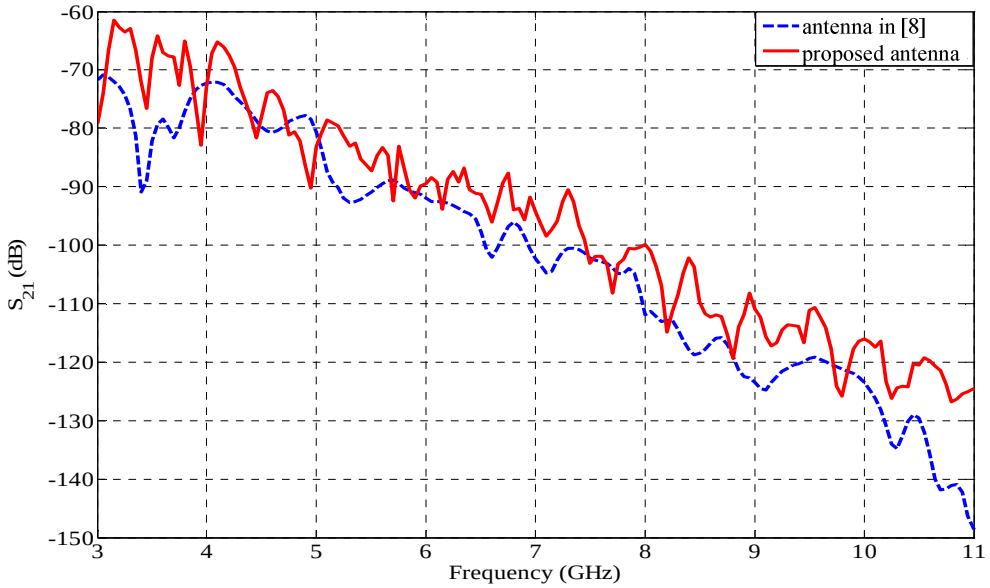

Fig. 2.2-9. Comparison of the transmission coefficients of the proposed antenna and the antenna in [8].

2.3 RASTER SCANNING SETUP

The antenna is used in the raster scanning setup introduced in [8]. There are two common data acquisition approaches in microwave imaging. The first approach utilizes scanning where usually one or two sensors perform a scan over the acquisition surfaces (e.g., see [18]-[21]). In the second approach, a fixed electronically switched array of sensors is used to sample the scattered field (e.g., see [22]). In both cases, the scattered field is usually sampled on canonical surfaces such as planes, cylinders or spheres, or portions of those. Also, the scattered field can be sampled at the location of the transmitter (monostatic case), at a location different from that of the transmitter (bistatic

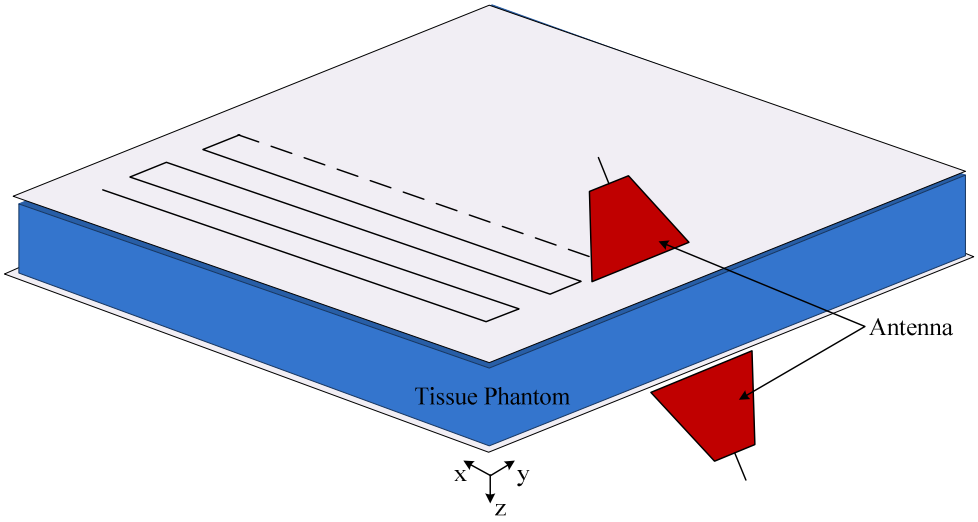

Fig. 2.3-1. Configuration of the raster scanning setup with two identical antennas

case) or at multiple locations (multistatic case).

The planar-raster scanning arrangement is shown in Fig. 2.3-1. Two Tx/Rx sensors (antennas) are placed along each other's boresight on both sides of the object. These sensors, together with the examined object, form a two-port microwave network whose *S*-parameters are measured at the desired frequencies. The two antennas are scanned simultaneously over the two planes. A flat phantom is used to emulate the human breast.

The measurements with the VNA produce the *S*-parameters of the two-port network, both the reflection and the transmission coefficients, as functions of *x* and *y*, which define the sampling position. Note that in this setup the antennas are fixed. It is the phantom which is being moved relative to the antennas by

the scanning table using two stepper motors. The scanned area of this system can extend up to 18 cm along x and y and the user-defined sampling step can be anywhere between 1 mm and 10 mm.

The performance of the new antenna compared to the antenna in [8] is investigated through a 1D scan of a tumor simulant of size 6 mm embedded in a 5 cm-thick tissue phantom. The properties of the tumor simulant and the tissue background are those of the tumor and fibroglandular tissues, respectively, presented in [8], with a contrast of 1.7 in permittivity and 10 in conductivity. Here, the contrast is defined as the ratio of the tumor property to that of the background. Fig. 2.3-2 shows the simulated transmission coefficients of the setup with the two antennas for the new and the previous designs at 3 GHz. As evident from the figure, $|S_{21}|$ is on average 2.5 dB higher for the new antenna in comparison with the previous one. In fact, the tumor cannot be detected when using the previous sensor design while $|S_{21}|$ measured with the new antennas contains a clear signature at the position of the tumor stimulant (inside the homogenous phantom). This confirms the improvement of the dynamic range and the sensitivity of the imaging setup due to the better antenna design which enables the detection of smaller tumor simulants in thicker tissue phantoms.

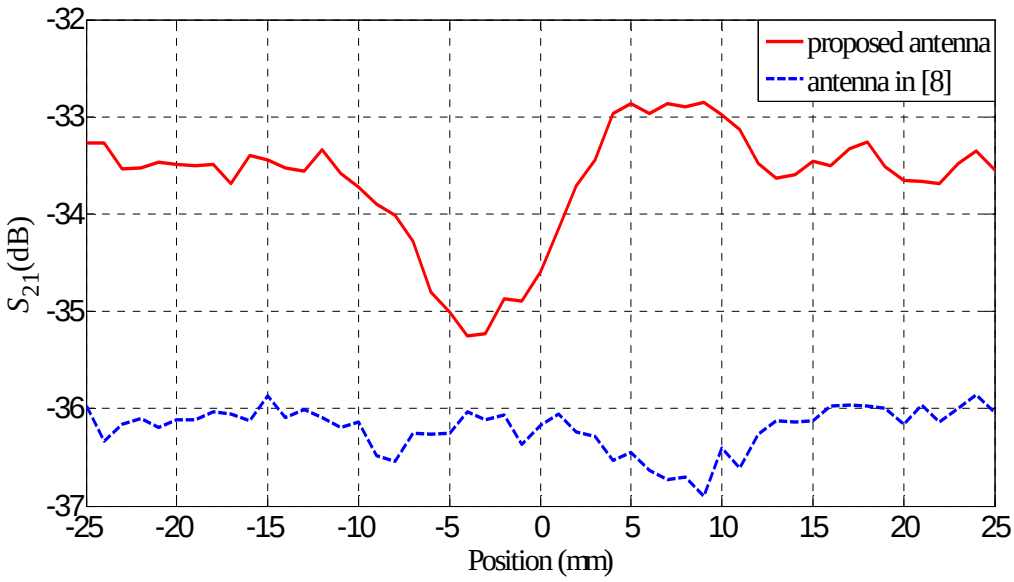

Fig. 2.3-2. Comparison of the tumor response for the new antenna with that for, the antenna in [8].

2.4 CONCLUSION

A new UWB TEM horn antenna is proposed for microwave tissue imaging. The advantage of this antenna over the previously proposed UWB TEM horn antenna is that the antenna is completely shielded. This ensures maximum coupling of the interrogating microwave power into the tissue. The investigated parameters of the antenna include the reflection coefficient and the coupling coefficient for a single antenna and the transmission coefficient in a setup where two antennas are placed on opposite sides of a compressed tissue phantom. These parameters demonstrate the satisfactory performance of the proposed antenna within the UWB. Excellent coupling efficiency is achieved that would increase the dynamic range of the raster scanning microwave

imaging setup. Moreover, the sensitivity of the imaging setup is increased, which enables the detection of smaller tumor simulants in thicker phantoms.

2.5 REFERENCES

[1] H. M. Jafari, M. J. Deen, S. Hranilovic, and N. K. Nikolova, "A study of ultrawide band antennas for near-field imaging," *IEEE Trans. Antennas Propag*., vol. 55, no. 4, pp. 1184–1188, Apr. 2007.

[2] H. M. Jafari, J. M. Deen, S. Hranilovic, and N. K. Nikolova, "Co-polarised and cross-polarised antenna arrays for breast, cancer detection," *IET Microwave Antennas Propag*., vol. 1, no. 5, pp. 1055–1058, Oct. 2007.

[3] D. A. Woten and M. El-Shenawee, "Broadband dual linear polarized antenna for statistical detection of breast cancer," *IEEE Trans. Antennas Propag*., vol. 56, no. 11, pp. 3576–3580, Nov. 2008.

[4] R. Nilavalan, I. J. Craddock, A. Preece, J. Leendertz, and R. Benjamin, "Wideband microstrip patch antenna design for breast cancer tumour detection," *IET Microwave Antennas Propag*., vol. 1, no. 2, pp. 277–281, Apr. 2007.

[5] H. Kanj and M. Popovic, "A novel ultra-compact broadband antenna for microwave breast tumor detection," *Progress In Electromagnetics Research, PIER* 86, pp. 169–198, 2008.

[6] X. Li, S. C. Hagness, M. K. Choi, and D. Van Der Weide, “Numerical and experimental investigation of an ultra-wideband ridged pyramidal-horn antenna with curved launching plane for pulse radiation,” *IEEE Antennas Wirel. Propag. Lett*., vol. 2, pp. 259–262, 2003.

[7] J. Zhang, E. C. Fear, and R. Johnston, “Cross-Vivaldi antenna for breast tumor detection,” *Microwave and Opt. Lett*., vol. 51, no. 2, pp. 275–280, Feb. 2009.

[8] R. K. Amineh, M. Ravan, A. Trehan, and N. K. Nikolova, “Near-field microwave imaging based on aperture raster scanning with TEM horn antennas,” *IEEE Trans. Antennas and Propag*., vol. 59, no. 3, pp. 928–940, Mar. 2011.

[9] J. W. Duncan and V. P. Minerva, “100:1 bandwidth balun transformer,” *Proc. Inst. Elect. Eng*., vol. 48, no. 2, pp. 156–164, Feb. 1960.

[10] P. R. Foster and S. M. Tun, “A wideband balun from coaxial line to TEM line,” *IEEE Int. Symp. Antennas and Propagation ICAP*, vol. 1, Eindhoven, The Netherlands, pp. 286–290, Apr. 1995.

[11] G. A. Mesyats, S. N. Rukin, V. G. Shpak, and M. I. Yalandin, “Generation of high-power subsecond pulses” *Ultra-wideband Short-Pulse Electromagnetics*, vol.4, Tel-Aviv, Israel, pp1–9, Jun. 1998.

[12] M. Lazebnik, M. Okoniewski, J. H. Booske, and S. C. Hagness, “Highly accurate Debye models for normal and malignant breast tissue dielectric

properties at microwave frequencies," *IEEE Microw. Compon. Lett.*, vol. 17, no. 12, Dec. 2007.

[13] Ansoft Corporation, http://www.ansoft.com.

[14] R. K. Amineh, A. Trehan, and N. K. Nikolova, "TEM horn antenna for ultra-wide band microwave breast imaging," *Progress In Electromagnetics Research B*, vol. 13, pp. 59–74, 2009.

[15] M. Lazebnik, L. McCartney, D. Popovic, C. B. Watkins, M. J. Lindstrom, J. Harter, S. Sewall, A. Magliocco, J. H. Booske, M. Okoniewski,and S. C. Hagness, "A large-scale study of the ultrawide band microwave dielectric properties of normal breast tissue obtained from reduction surgeries," *Phys. Med. Biol.*, vol. 52, pp. 2637–2656, May 2007.

[16] A. Trehan, *Numerical and physical models for microwave breast im aging*, M.A.Sc. Thesis, McMaster University, 2009.

[17] Emerson & Cuming Microwave Products, http://www.eccosorb.com.

[18] Y. Zhang, S. Tu, R.K. Amineh, and N.K. Nikolova, "Sensitivity-based microwave imaging with raster scanning," *IEEE MTT-S Int. Microwave Symp.*, June 2012.

[19] L. E. Larsen, and J. H. Jacobi, Medical Applications of Microwave Imaging. New York: IEEE Press, 1986.

[20] E. Fear, X. Li, S. C. Hagness, and M. A. Stuchly, “Confocal microwave imaging for breast cancer detection: localization of tumors in three dimensions,” *IEEE Trans. Biomed. Eng.*, vol. 49, no. 8, pp. 812–822, Aug. 2002.

[21] Z. Q. Zhang, and Q. H. Liu, “Three-dimensional nonlinear image reconstruction for microwave biomedical imaging,” *IEEE Trans. Biomed. Eng*., vol. 51, no. 3, pp. 544–548, Mar. 2004.

[22] T. Rubaek, P. M. Meaney, P. Meincke, and K. D. Paulsen, “Nonlinear microwave imaging for breast-cancer screening using Gauss–Newton’s method and the CGLS inversion algorithm,” *IEEE Trans. Antennas Propag.*, vol. 55, no. 8, pp. 2320–2331, Aug. 2007.

Chapter 3

Estimating the Efficiency of Antennas Used as Sensors in Microwave Tissue Measurements

3.1 INTRODUCTION

The efficiency of the sensor affects the efficiency and the dynamic range of the imaging system. The system noise temperature of the receiving antenna T_{sys} is related to its losses and, therefore, to its radiation efficiency η. In the absence of external noise sources, the relationship between T_{sys}, the antenna efficiency, and the ambient temperature of the antenna T_{amb} is [1]:

$$T_{sys} = T_{amb}(1-\eta)/\eta\,. \tag{3.1}$$

Methods to estimate the efficiency of the microwave tissue sensors using full-wave simulations have been reported before [2], [3]. Such approaches are

not satisfactory bearing in mind the possibility of low fidelity of the simulation of the tissue imaging setup. The measurement approach has the advantage of including all of the hidden loss factors that may not be included in the simulation. Examples might include poor solder joints, a lossy film on the conductors, or losses in tuning and matching components. Therefore, it is preferable to have a method based on measurements.

So far, both the radiation and the coupling efficiencies of microwave-imaging antennas have been evaluated through full-wave simulations. The radiation efficiency [4] describes the intrinsic conduction and dielectric losses of the antenna. In contrast, the coupling efficiency describes the sensor's ability to channel the available microwave power toward the tissue [2] without loss, i.e., it takes into account not only the intrinsic loss, but also the return loss and the loss due to power leakage away from the tissue. It can be computed from the radiation efficiency if the return loss and the field pattern are known. In general, estimating the radiation efficiency is an ongoing challenge, particularly for antennas operating in environments other than free space and especially in heterogeneous media such as tissue.

One common method for estimating the efficiency of antennas used in communications is the Wheeler-cap method, originally proposed in [5] and revisited many times; see, e.g., [6]. The method cannot be used to evaluate the efficiency of tissue sensing antennas. First, it is not suitable for lossy media

because it cannot separate the tissue loss from that of the antenna. Second, it is not applicable to ultrawide-band (UWB) antennas (many tissue-sensing antennas have very wide bandwidths). The size of the Wheeler cap depends on the frequency of interest—its radius must be $r \approx \lambda/2\pi$, where λ is the wavelength (see Fig. 3.1-1). This ensures that the cap is big enough not to disturb the antenna current distribution and small enough to suppress resonant modes. Attempts have been made to modify the Wheeler-cap method for broadband applications [7]-[9]. However, it has been shown in [10] that accurate efficiency values cannot be obtained at all frequencies especially due to resonant modes in the cap and the associated increased cap loss. Third, the Wheeler cap method is practical only for electrically small antennas (smaller than a wavelength).

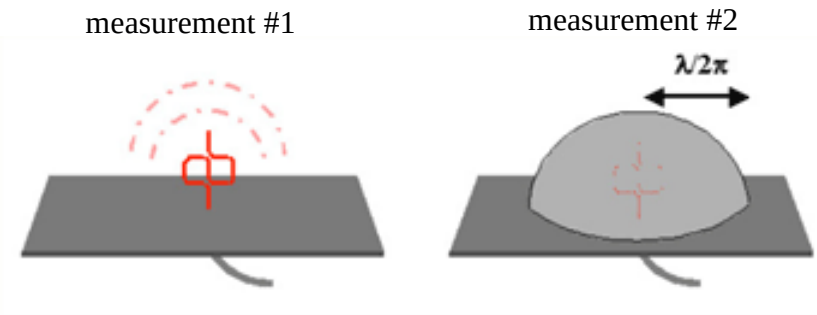

Fig. 3.1-1. Wheeler cap method [http://www.tsc.upc.es/fractalcoms/t43.htm]

Another classical method is the gain/directivity method [11]. It is only suitable for antennas operating in free space. Also, it is expensive in terms of

equipment and time.

More recently, the reverberation chamber was introduced as a new facility for measuring the antenna efficiency in multipath environments; see, e.g., [12]. The purpose of the reverberation chamber is the generation of a statistically uniform, isotropic and randomly polarized field. This method, too, cannot separate the tissue loss from the antenna loss. As with the Wheeler-cap method, the antenna could be measured without the tissue inside the chamber; however its current distribution would be substantially different from that in its intended application and the loss result will be invalid. On the other hand, if the antenna was measured with the tissue inside the chamber, the loss of the tissue would be added to that of the antenna.

In [13], the antenna is represented as a two-port network and its efficiency is expressed in terms of the scattering parameters of this network. The measurements are performed with the antennas placed in a waveguide so that their current distribution is not disturbed significantly. Consequently, the approach is only suitable for small antennas operating in air. Conceptually, this method follows the Wheeler-cap approach and, therefore, shares similar limitations.

In this chapter, we propose a new method for evaluating the efficiency of antennas employed in tissue imaging, including those operating in direct contact with the tissue. To our knowledge, such method is being proposed for

the first time. It is based on measurements with two samples of the same antenna operating in their intended environment, e.g., with a tissue phantom between them. Similarly to [13], the antenna is represented by the scattering parameters of an equivalent two-port network, from which the efficiency is calculated. In our method, however, these scattering parameters are extracted differently, so that the tissue loss can be effectively separated from the antenna loss. The proposed method is suitable for electrically large as well as UWB antennas. Also, it can be applied with any tissue phantom (solid or liquid) as needed by the particular antenna. Due to the versatility of the technique, it could be employed to evaluate free-space antennas as well.

3.2 EVALUATION OF THE ANTENNA EFFICIENCY

The antenna is modelled as a two-port network represented by its four generalized scattering parameters as shown in Fig. 3.2-1. As the characteristic impedances at the input and output ports are not the same, general scattering parameters are needed. The impedance Z_f at the input port is that of the feed line while the impedance Z_m at the output port is the intrinsic impedance of the radiation medium.

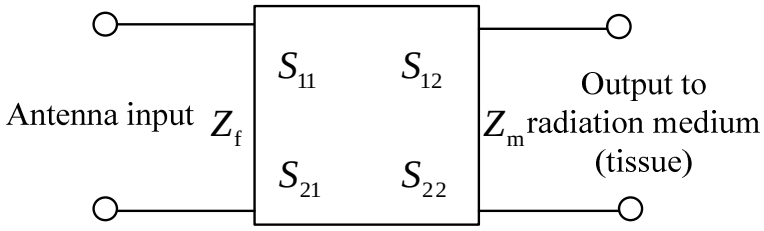

Fig. 3.2-1. The antenna as a two-port network.

3.2.1 **Radiation Efficiency and Antenna Network Parameters**

The radiation efficiency η is defined as the ratio of the total radiated power P_r to the power accepted by the antenna P_o [4]:

$$\eta = \frac{P_r}{P_o}. \tag{3.2}$$

Considering the reflection at the antenna terminals, the relation between P_o and the input power P_{in} can be expressed as

$$\frac{P_o}{P_{in}} = 1 - |S_{11}|^2. \tag{3.3}$$

Since the antenna is a passive two-port network, its loss power P_l can be related to the input power in terms of the scattering parameters as

$$\frac{P_l}{P_{in}} = 1 - |S_{11}|^2 - |S_{21}|^2. \tag{3.4}$$

Then, the efficiency is written in terms of P_l, P_o, and P_{in} as

$$\eta = \frac{P_r}{P_o} = \frac{P_o - P_l}{P_o} = \frac{P_o/P_{in} - P_l/P_{in}}{P_o/P_{in}} \tag{3.5}$$

which leads to

$$\eta = \frac{\left|S_{21}\right|^2}{1-\left|S_{11}\right|^2}. \tag{3.6}$$

3.2.2 **Measurement Setup and Signal Flow Graph**

The scattering parameters $\left|S_{21}\right|$ and $\left|S_{11}\right|$ are needed in (3.6) for the antenna efficiency estimation. For this purpose, a measurement setup is proposed in which we employ two identical antennas facing each other, with the tissue medium (radiation medium) between them as shown in Fig. 3.2-2. The medium between the two antennas is modeled as a transmission component in the signal flow graph (SFG) of the complete network; (see Fig. 3.2-3). The antennas are represented by their four unknown *S*-parameters in the SFG while the tissue medium is represented by the complex parameter m_t, which is also unknown. This parameter depends on the signal path and on the tissue losses as well as on the field distribution in the medium between the antennas. Note that in near-field imaging, standing waves are possible, which results in power loss different from that in a traveling wave field distribution. All 5 unknown SFG parameters must be estimated using measurements.

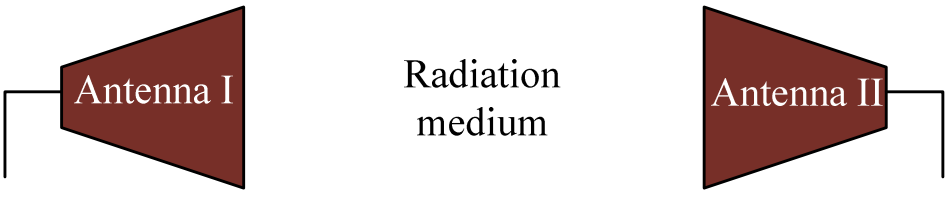

Fig. 3.2-2. Two identical antennas with a radiation medium between them.

The complete SFG is characterized by the *S*-parameters of the equivalent two-port network of the setup (see Fig. 3.2-3) when matched to 50-Ω loads. These *S*-parameters are measured with a vector network analyzer (VNA). The SFG can be solved to express the measured *S*-parameters, $\overline{S}_{11}^{\mathrm{ML}}$ and $\overline{S}_{21}^{\mathrm{ML}}$ (superscript "ML" indicates matching to 50-Ω loads at the ports), in terms of the unknowns S_{11}, S_{12}, S_{21}, S_{22} and m_t:

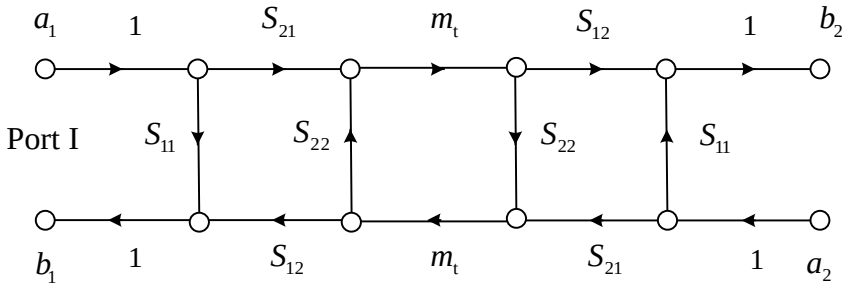

Fig. 3.2-3. The SFG of two identical antennas with a radiation medium between them.

$$\overline{S}_{11}^{\mathrm{ML}} = S_{11} + S_{12}S_{21}\frac{m_t^2 S_{22}}{1 - m_t^2 S_{22}^2} = \overline{S}_{22}^{\mathrm{ML}} \tag{3.7}$$

$$\overline{S}_{21}^{\mathrm{ML}} = \frac{S_{12}S_{21}m_t}{1 - m_t^2 S_{22}^2}. \tag{3.8}$$

From the reciprocity principle, it follows that S_{12}=S_{21}. Therefore, there are four unknowns in the system of equations formed by (3.7) and (3.8). To solve for these four unknowns, at least two extra equations are required.

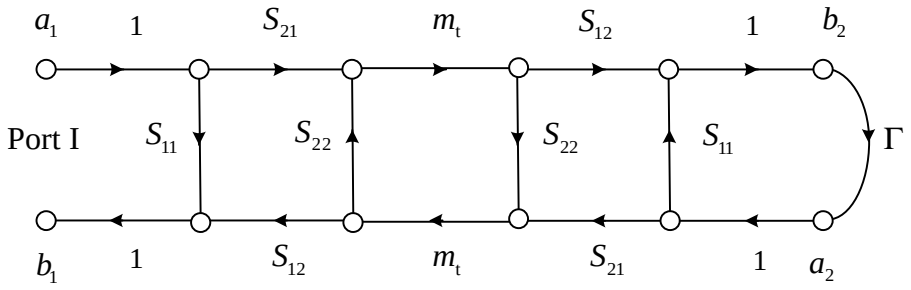

Fig. 3.2-4. The SFG of two identical antennas with a radiation medium between them when an arbitrary load of reflection coefficient Γ is connected to the terminals of antenna II.

Two additional equations can be obtained by connecting known loads to port II, represented by Γ in the SFG shown in Fig. 3.2-4. The expression for the reflection *S*-parameter at the terminals of antenna I is obtained as

$$\overline{S}_{11}^{\Gamma} = S_{11} + \frac{S_{12}S_{21}m_t^2\left(S_{22} - \Gamma S_{11}S_{22} + \Gamma S_{12}S_{21}\right)}{1 - \Gamma S_{11} - S_{22}^2 m_t^2 + \Gamma S_{11}S_{22}^2 m_t^2 - \Gamma S_{12}S_{21}S_{22}m_t^2}. \tag{3.9}$$

With two loading conditions, $\Gamma = \pm 1$ (open and short circuits), two additional equations are obtained, for $\overline{S}_{11}^{\mathrm{OC}}$ and $\overline{S}_{11}^{\mathrm{SC}}$. Here, the superscripts OC and SC stand for open circuit and short circuit, respectively. Thus, a system of four nonlinear equations with four unknowns is constructed using (3.7), (3.8) and (3.9).

It is worth noting that if the antennas are located in each other's far zone, connecting different loads at the terminals of antenna II produces insignificant changes on the measured reflection *S*-parameters at the terminals of antenna I. On the other hand, when the antennas are in each other's reactive zones, the current distributions on the antenna structures suffer undesired changes. This in

turn affects the efficiency of the antennas as compared to their normal operating conditions (when only the tissue medium is in front of the antenna).

To avoid the aforementioned problems, as a trade-off, measurements are performed in the Fresnel zone. The boundary between the reactive near zone and the Fresnel zone can be estimated by the well-known expression $0.62(D^3/\lambda)^{1/2}$. Note that the calculation of the wavelength λ must take into account the conductivity and the permittivity of the medium where the antennas are placed. In practice, the separation distance has to be further adjusted from the initially estimated Fresnel-zone boundaries by performing several measurements (with short and open loads at the antenna II terminals), starting from the far zone and gradually decreasing the distance between the antennas until the difference between $\overline{S}_{11}^{SC}$ and $\overline{S}_{11}^{OC}$ becomes measureable, i.e., it is considerably larger than the measurement noise. Since these boundaries depend on the frequency, in the UWB case, several measurements may be required in the different frequency sub-bands. In general, the wider the frequency band is, the more measurement sets are required in sufficiently narrow sub-bands.

Furthermore, to have better estimation of m_t and to reduce the effects of measurement noise and uncertainty, it is better to have extra measurements performed at various distances in the Fresnel zone. Then, the nonlinear system

of equations is over-determined and it is solved in the least-square sense.

3.2.3 **Solving the Nonlinear System of Equations**

To solve the least-square problem, the initial solutions are obtained with the genetic algorithm in the Matlab optimization toolbox [14]. Then, starting from the solution provided by the genetic algorithm, the SFG parameters are optimized further using the Levenberg-Marquardt algorithm with a line search [14]]. This approach is based on various studies showing that the combination of local and global optimization methods results in a faster and better solution [15]]-[17]. The genetic algorithm is in principal capable of finding a global solution; however, it is slow to converge once the neighborhood of the global optimum is found. In the genetic-local hybrid, the main role of the genetic algorithm is to explore the search space in order to isolate the most promising region. On the other hand, the role of the local search method is to locate quickly the local optimum in this region, thereby refining the solution found by the genetic algorithm. In the examples presented below, the target values achieved by the genetic optimization were reduced by an average of 30% by performing the additional local optimization. Moreover, the genetic-algorithm performance strongly depends on the population size as well as the cross-over and mutation probabilities. We optimized those values to achieve smaller target value with fewer iterations as follows: population size is 200, cross-over probability is 0.9 and mutation probability is 0.2.

To reduce the nonuniqueness of the solution and to ensure convergence toward the true solution for the antenna loss, four constraints are used.

The first constraint is:

$$|S_{11}|^2 + |S_{21}|^2 \le 1 \tag{3.10}$$

which follows from the conservation of power for the passive two-port network.

The second constraint restricts the behavior of the magnitude of the complex transmission parameter $|m_t|$ as a function of the distance D between the two antennas:

$$\left| \frac{|m_t^{(n)}|}{|m_t^{(m)}|} - R_{nm} \right| \le \delta_a \cdot R_{nm} \tag{3.11}$$

where

$$R_{nm} = \frac{e^{-\alpha\left(D^{(n)} - D^{(m)}\right)}}{D^{(n)} / D^{(m)}}. \tag{3.12}$$

Here, the relative difference δ_a is a small real positive number. In (3.11), the superscripts n and m are indicates that measurements performed at distances $D^{(n)}$ and $D^{(m)}$, respectively, where $m \ne n$. In (3.12), α is the attenuation constant calculated from the known conductivity (or loss tangent) of the radiation medium. Thus, R_{nm} estimates the signal-attenuation ratio for spherical-wave propagation in a lossy medium. The constraint (3.11) in effect forces the optimization to search for a solution of $|m_t|$ close to a behavior

described by $|m_t| \sim e^{-\alpha D}/D$. The propagation mechanism does not need to be necessarily spherical as assumed by the ratio in (3.12). However, if the measurements are performed in an unbounded lossy medium and in the Fresnel zone of the antennas, this approximation of the R_{nm} dependence on distance is adequate. If the behavior of the signal attenuation is expected to be significantly different from that of a spherical wave, then the ratio (3.12) should be properly adjusted, e.g., using simulated models. To allow for sufficient freedom in the $|m_t|$ behavior, δ_a should not be too small. In all our examples, $\delta_a = 0.2$.

The third constraint is

$$\left| \angle m_t^{(n)} - \angle m_t^{(m)} - \beta\left(D^{(n)} - D^{(m)}\right) \right| \le \delta_\varphi \tag{3.13}$$

in which β is the medium's phase constant. This constraint imposes restrictions on the phase delay of the signal traveling through the radiation medium. Similarly to the previous constraint, it assumes reflection-free propagation. The choice of the deviation δ_φ depends on the accuracy of this assumption. In all our examples, $\delta_\varphi = \pi/10$.

The fourth and final constraint is:

$$\left|S_{11}\right| - \left|S_{11}^{\text{single}}\right| \le \delta_r \tag{3.14}$$

where S_{11}^{single} is the measured reflection coefficient of a single antenna with the tissue medium. In this single-antenna measurement, the thickness of the tissue medium must be large enough so that the reflections from its further end are negligible at the antenna port. This constraint is based on the expectation that the presence of a second antenna in the Fresnel region of the first one cannot significantly alter the magnitude of the first antenna's reflection coefficient. The recommended value of δ_{r} is 0.2.

3.3 VALIDATION AND RESULTS

As an example, the proposed method is employed to evaluate the efficiency of a UWB antenna [2]. The antenna was developed for breast-cancer diagnostics. It has been designed to operate in direct contact with the tissue. The performance of this antenna, its efficiency included, is highly frequency-dependent and so are the properties of the tissue phantom.

Fig. 3.3-1 shows the measured properties of the material used to make the tissue-phantom slabs placed between the two antennas in the measurements. The same properties are used in the simulations of the respective setups.

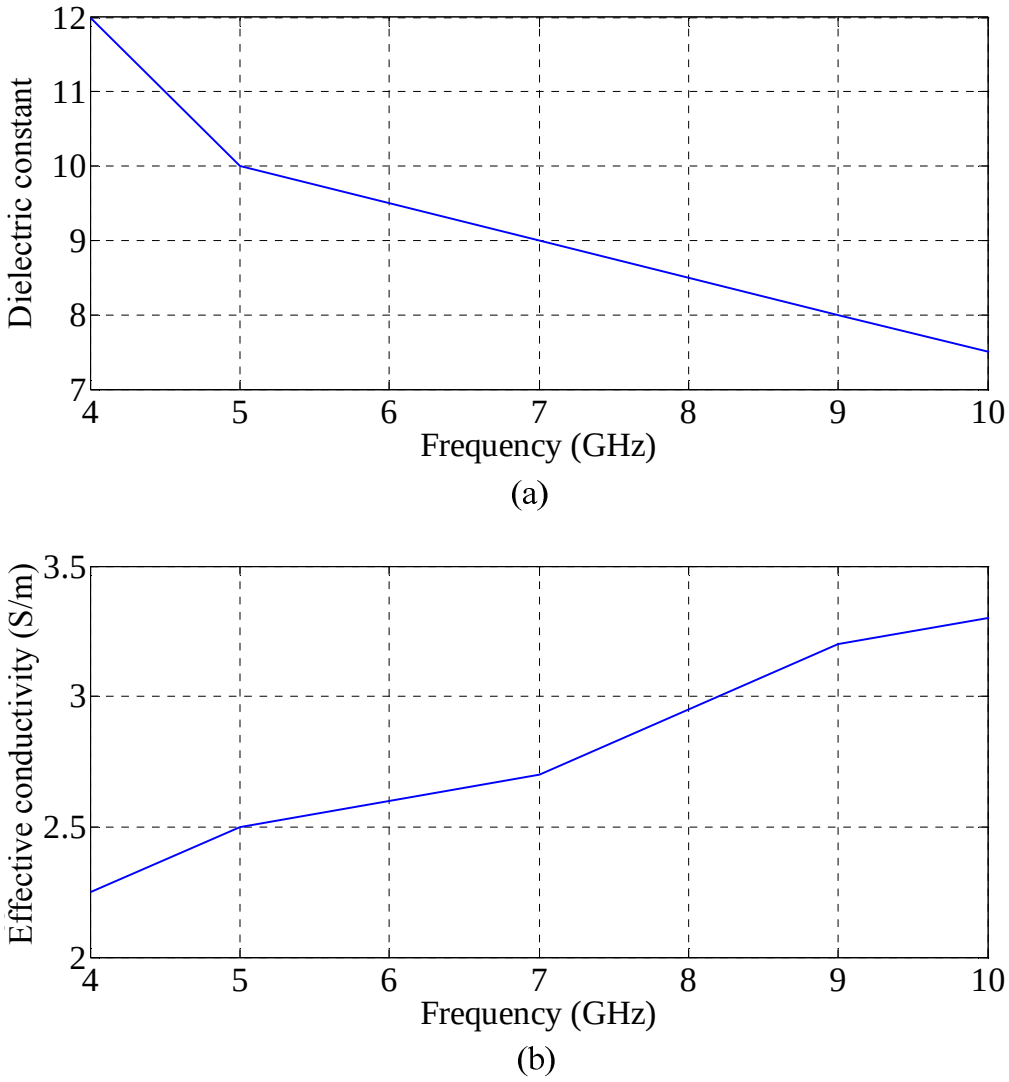

Fig. 3.3-1. Measured constitutive parameters of the tissue layers made of glycerin phantoms (the same properties are employed in the HFSS simulations): (a) dielectric constant and (b) effective conductivity.

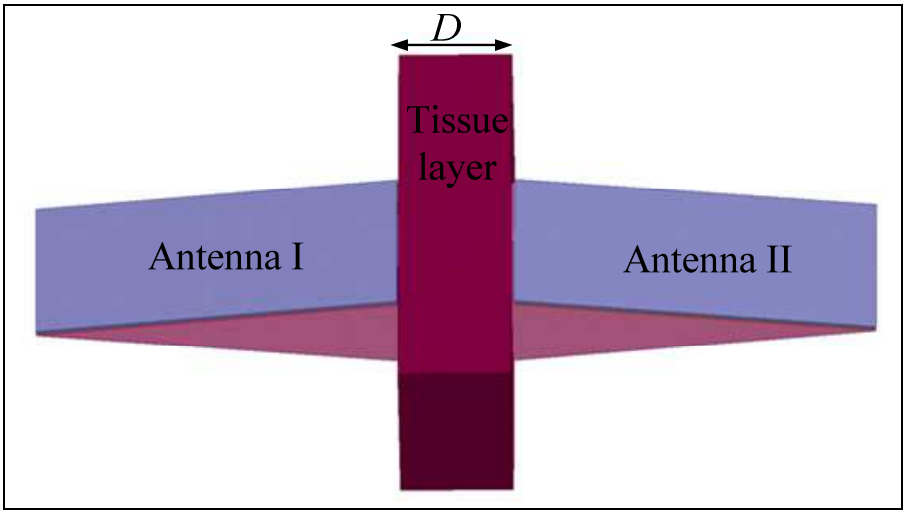

Fig. 3.3-2. Simulation setup consisting of the two TEM horn antennas proposed in [2] and a tissue layer with a thickness of *D* between them.

The accuracy of the proposed method in evaluating the efficiency of this antenna is examined via simulated and measured data. Fig. 3.3-2 shows the simulation configuration of the two TEM horn antennas with a tissue layer of thickness *D* between them. The full-wave simulations of all different scenarios under matched load, open circuit, and short circuit for four distances between the two antennas are performed in HFSS ver. 13 [18]. The four distances are: 2 cm, 3 cm, 5 cm and 7 cm. The computational domain is terminated by radiation boundary conditions, the sides of the tissue layer included. The phantom properties are simulated as per the measured data in

Fig. 3.3-1.

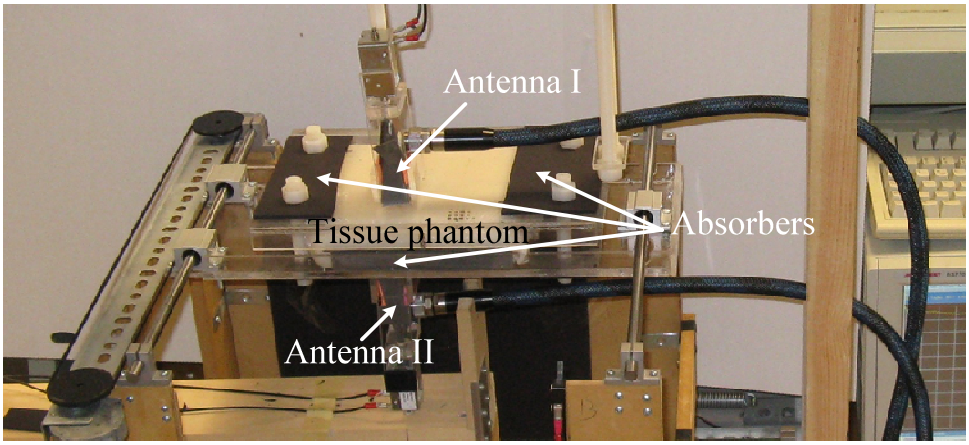

Fig. 3.3-3. Photo of the measurement setup for two antennas with a tissue layer between them.

A photo of the respective measurement setup is shown in Fig. 3.3-3. Absorbers are placed around the phantom to reduce the interference and reflections. The measurements have been performed with a Vector Network Analyzer (VNA) Advantest-R3770 where the resolution bandwidth (RBW) is 10 kHz, the averaging factor is 10 and the input power is 8 dBm. The four different distances are realized with four tissue phantoms of thicknesses 2 cm, 3 cm, 5 cm and 7 cm. The phantoms are solid slabs the transverse size of which is 10 cm by 10 cm. The slabs are homogeneous with electrical parameters as in

Fig. 3.3-1.

Fig. 3.3-4 shows the calculated efficiency of the antenna versus frequency where four results are being compared. First, the proposed method is applied

with the measured *S*-parameters acquired with the four tissue phantoms. Second, the proposed method is applied with the respective simulated *S*-parameters. The figure also shows two numerically computed efficiency curves based on field information extracted from the full-wave simulations. This computation employs the ratio of radiated to accepted power. The radiated power is obtained through the integration of the normal component of the real part of the Poynting vector over a closed surface tightly enveloping the antenna. The accepted power is the input power at the port (1 W) multiplied by ($|1-|S_{11}|^2$), see (3.3). The third curve shows the results when this computation is performed in all four simulations of the two-antenna acquisition setup with the four different phantom thicknesses and the average is taken. In these simulations, the two antennas are matched to 50-Ω loads. The fourth curve shows the result when this computation is performed in the simulation of a single antenna attached to a semi-infinite phantom. On average, satisfactory agreement is observed between all results. However, there are observable differences, which are discussed in more detail below.

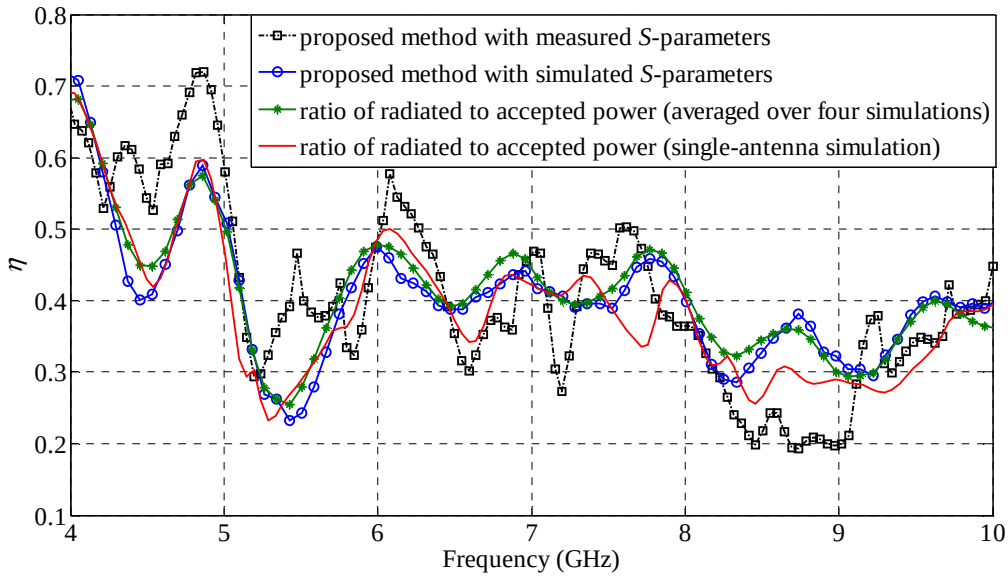

Fig. 3.3-4. Comparison of the efficiency of the antenna in [2] evaluated by: (i) the proposed method using measured data, (ii) the proposed method using simulated data, (iii) the average of the ratios of the radiated to accepted power computed in the 4 simulations with 4 different slab thicknesses, and (iv) the ratio of the radiated to accepted power computed in the simulation of a single antenna attached to a semi-infinite tissue region.

First, we discuss the differences between the efficiency values based on the measurements with four slabs of different thicknesses and those based on the simulations of these measurements. These differences are due to the inaccuracies in the simulations modeling the actual measurement setup. For example, the absorbing sheets, which in reality are not perfectly matched to the phantom, are simply simulated by an absorbing boundary condition. The details in the connectors are also not fully represented. The simplifications in the simulation model are necessitated by the otherwise prohibitive computation time. There are significant differences between the simulated and the measured

S-parameters for the two-antenna setup with each slab thickness (not shown for brevity). The absolute differences between these two sets of *S*-parameters are on average 0.15 (linear scale) between 8 GHz and 9 GHz (the frequency range of the worst disagreement). Consequently, the efficiency values obtained with these two sets of data differ by as much as 0.18 (again in absolute terms). In summary, the difference in the efficiency estimates based on measured and simulated *S*-parameters is due to the difference between the *S*-parameters themselves.

To confirm the validity of the proposed method in the case of simulated *S*-parameter data, we exploit the fact that in simulations the field distribution is available and can be used to compute the efficiency as the radiated-to-accepted power ratio as explained before. This method has been used to compute the efficiency in the four simulations of the two-antenna setup (with the four slab thicknesses) under matched-load conditions and the results were averaged to produce the third curve in Fig. 3.3-4. This curve agrees much better with the curve obtained from the simulated *S*-parameters processed by the proposed method.

The fourth curve in Fig. 3.3-4 shows the efficiency calculated as the radiated-to-accepted power ratio in the simulation of a single antenna attached to a semi-infinite slab. As expected, this result is somewhat different from the

third curve. This is due to two major differences between the two-antenna and the single-antenna simulations: (i) finite-thickness slabs in the former case versus a semi-infinite slab in the latter case, and (ii) the effect of the second antenna on the reflection coefficient of the first antenna in the former case while the second antenna is simply not present in the latter case. It is important to note that the differences in these two results are representative of the accuracy expectation for the proposed approach, which is based on two-antenna measurements while, in practice, the acquisition method may be using a single antenna. Since in the two-antenna measurements the two antennas are in each other's Fresnel zone, they affect each other's current distributions. However slight this effect may be, it does influence the efficiency estimates.

As a second example, the efficiency of a printed tapered square monopole antenna fed with a coplanar waveguide (CPW) is investigated. The antenna has been originally proposed in [19] for breast-cancer detection. It is designed to operate in a lossy coupling liquid. Its frequency range is from 3 GHz to 10 GHz. Fig. 3.3-5 shows the simulation setup with two printed monopoles immersed in the liquid.

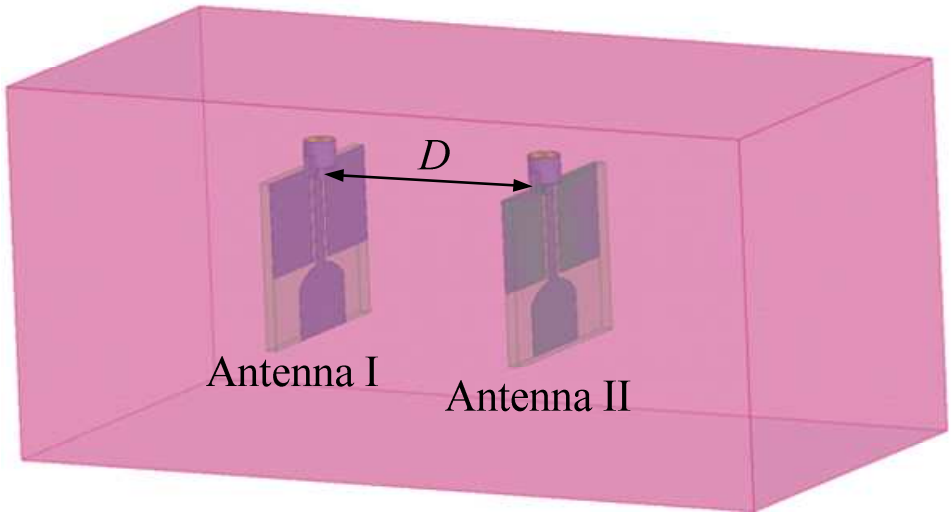

Fig. 3.3-5. Simulation setup of the two printed square monopoles [19] located inside a liquid phantom.

Measurements are performed at four distances between the two antennas: 2 cm, 3 cm, 5 cm and 7 cm. The distance between the antennas is adjusted by moving the antennas in the tank (the tank is 15 cm deep, 25 cm wide and 35 cm long). The properties of the liquid are similar to those shown in

Fig. 3.3-1. The VNA setup is the same as in the previous example.

Fig. 3.3-6 compares the estimated efficiency values for this antenna versus frequency. The four curves are obtained in the same manner as in the first example. The results are generally in good agreement. As expected, the agreement among the last three curves that are based on simulations is better than that between the first curve (results based on measured *S*-parameters) and the second curve (results based on simulated *S*-parameters). Similarly to the

first example, the latter comparison is less favorable because of the insufficient fidelity of the simulations modeling the rather complex measurement setup whereby the differences in the measured and simulated *S*-parameters lead to differences in the respective efficiency estimates.

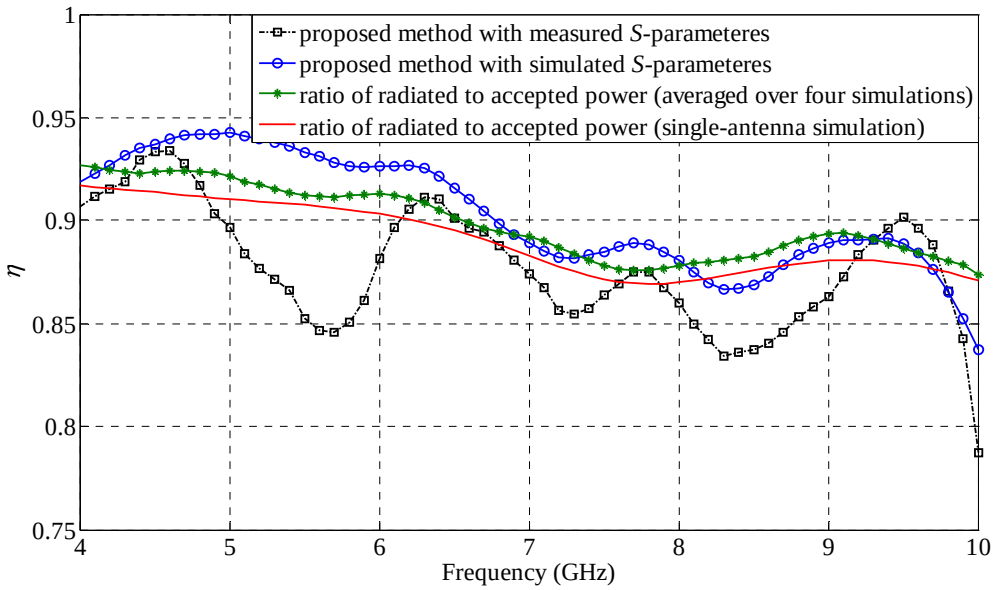

Fig. 3.3-6. Comparison of the efficiency of the antenna in [18] evaluated by: (i) the proposed method using measured data, (ii) the proposed method using simulated data, (iii) the average of the ratios of the radiated to accepted power computed in the 4 simulations with 4 different slab thicknesses, and (iv) the ratio of the radiated to accepted power computed in the simulation of a single antenna radiating into a semi-infinite tissue region.

3.4 CONCLUSION

A measurement-based method is proposed for evaluating the efficiency of antennas used in tissue imaging. The method models the antenna as a two-port network. It uses two identical antennas in a measurement setup where either

solid or liquid tissue phantoms are employed. A signal flow graph models the measurement, facilitating the relation between the measured *S*-parameters and the antenna efficiency. The method is also applicable to antennas working in free space or any other open medium. The accuracy of the method has been validated in tests involving two different types of antennas designed for microwave tissue imaging. The results are in good agreement with the simulated efficiencies. The proposed method brings two benefits into the field of antenna measurements: (i) a measurement-based technique to evaluate the efficiency of antennas operating in a complex (layered, lossy, dispersive) medium and in a very wide bandwidth; (ii) the ability to compare the performance of antennas used in tissue sensing in terms of their efficiencies.

3.5 REFERENCES

[1] R. Maaskant, D. J. Bekers, M. J. Arts, W. A. van Cappellen, and M. V. Ivashina "Evaluation of the radiation efficiency and the noise temperature of low-loss antennas," *IEEE Antennas Wireless Propag. Lett*., vol. 8, pp. 1536−1225, Nov. 2009.

[2] R. K. Amineh, M. Ravan, A. Trehan, and N. K. Nikolova, "Near-field microwave imaging based on aperture raster scanning with TEM horn antennas," *IEEE Trans. Antennas Propag*., vol. 59, no. 3, pp. 928−940, Mar. 2011.

[3] H. Kanj and M. Popovic, “Miniaturized microstrip-med “dark eyes” antenna for near-field microwave sensing,” *IEEE Antennas Wireless Propag. Lett*., vol. 4, pp. 397–401, 2005.

[4] “IEEE standard definitions of terms for antennas,” IEEE Std 145-1993, p. i, 1993.

[5] H. A. Wheeler, “The radiansphere around a small antenna,” *Proc. IRE*, vol. 47, no. 8, pp. 1325−1331, Aug. 1959.

[6] S. Agahi and W. Domino, “Efficiency measurements of portable-handset antennas using the Wheeler cap,” *Applied Microwave & Wireless*, vol. 12, pp. 34–42, 2000.

[7] H. Schantz, *The Art and Science of UWB Antennas*. Norwood, MA: Artech House, 2005, ISBN: 1-58053-88-6.

[8] G. L. Fur, C. Lemoine, P. Besnier, and A. Sharaiha, “Performances of UWB Wheeler Cap and reverberation chamber to carry out efficiency measurements of narrowband antennas,” *IEEE Antennas Wireless Propag. Lett*., vol. 8, pp. 332–335, 2009.

[9] M. Huynh, *Wideband Compact Antennas for Wireless Communication Applications*. Ph.D. Thesis, Virginia State Univ., 2004.

[10] Y. Huang, Y. Lu, S. Boyes, H. T. Chattha, and N. Khiabani, “Wideband antenna efficiency measurements,” *IEEE International Workshop on Antenna Technology* (iWAT) 2010, Lisbon.

[11] C. A. Balanis, Antenna Theory: Analysis and Design. New York: Harper and Row, 1982.

[12] C. L. Holloway, H. Shah, R. J. Pirkl, W. Young, D. A. Hill, and J. Ladbury, "New reverberation chamber techniques for determining the radiation and total efficiency of antennas," *IEEE Trans. Antennas Propag*., vol. 60, no. 4, pp. 1758–1770, Apr. 2012.

[13] R. H. Johnston and J. G. McRory, "An improved small antenna radiation-efficiency measurement method," *IEEE Antennas Propag. Mag.*, vol. 40, no. 5, pp. 40–48, Oct. 1998.

[14] Matlab7.1 ed. Natick, MA, The MathWorks, Inc., 2005.

[15] T. Bilnder, C. Heitzinger, and S. Selberherr, "A study on global and local optimization techniques for TCAD analysis tasks," *IEEE Trans. Computer-aided Des. Integr. Circuits Syst*., vol. 23, no. 6, Jun. 2004.

[16] T. A. El-Mihoub, A. A. Hopgood, L. Nolle, and A. Battersby, ''Hybrid genetic algorithms: a review,'' *Engineering Letters*, vol. 3, no. 2, pp. 124–137, 2006.

[17] P. Preux and E.-G. Talbi, "Towards hybrid evolutionary algorithms," *International Transactions in Operational Research*, vol. 6, pp. 557–570, 1999.

[18] Ansoft Corporation [Online]. Available: http://www.ansoft.com

[19] H. M. Jafari, M. J. Deen, S. Hranilovic, and N. K. Nikolova, “Co-polarized and cross-polarized antenna arrays for breast cancer detection,” IET Microw. Antennas Propag., vol. 1, no. 5, pp. 1055–1058, Oct. 2007.

Chapter 4

Sensitivity of microwave imaging systems employing scattering-parameter measurements

4.1 INTRODUCTION

So far the antenna efficiency has been considered as an important performance metric of sensor in microwave imaging as it has strong impact on the sensitivity of a MWI system. On the other hand, to our knowledge, no method has been introduced so far to quantify the performance of a MWI system in terms of its sensitivity. The purpose of this chapter is to propose a definition and a method to evaluate the sensitivity of microwave imaging systems.

Imaging is essentially a two-stage process in which the first stage involves the acquisition of the signals in a radiation stream and the second stage involves the extraction of information from this stream, including the reconstruction algorithm, the image processing, formatting, and interpretation. At the acquisition stage, the raw data is collected. The raw-data quality is critical for the final image fidelity and it can be assessed independently from the reconstruction or the image-processing algorithms. It is desirable to be able to assess and quantify the physical merits of the data-acquisition hardware in order to design it efficiently and to compare it to other systems.

In [1], Wagner *et al*. introduced the signal-to-noise ratio of an ideal observer (SNRI). They presented expressions for the SNRI of all the major medical imaging modalities at the time, including radiography, computed tomography (CT), nuclear magnetic resonance (NMR), and PET (positron emission tomography), along with ways to use this expression as a figure of merit. The primary figure of merit is referred to as the physical sensitivity of a medical imaging setup. The method of obtaining the SNRI and the physical sensitivity needs rigorous statistical analysis of the inspected system. It was developed further and was applied to other medical imaging modalities in [2]-[5]. Microwave imaging systems have not yet been used in wide clinical practice and, to our knowledge, there are no rigorous or common means to quantify their performance in terms of physical sensitivity.

The objective here is to define what physical sensitivity means in the case of microwave imaging of tissue and to propose methods to estimate it. The proposed approach is different from common signal-to-noise image assessments. Since microwave imaging relies on the permittivity contrast between the scattering objects and their background, the proposed methodology estimates the smallest detectable change in the complex permittivity per unit volume in the background. The measurement uncertainty at the acquisition stage can be determined and it is a good indicator of the quality of the raw data. Then, the *physical contrast sensitivity* (PCS) is defined as a figure of merit. Methods to estimate the PCS through simulations and through measurements are also proposed.

The PCS is not only useful in comparing the different acquisition systems but can also be used as an optimization goal during the sensor design. For example, in microwave tissue imaging, the sensor design includes goals such as high efficiency, wide bandwidth, small size, reduced inter-sensor coupling, etc. These goals by themselves do not guarantee the best detection ability of the whole system although they do affect it. On the other hand, the PCS can play the role of an aggregate performance measure of the sensor detection ability.

Improving the PCS of a single sensor during its design—typically done through simulations—does not necessarily mean the best PCS of the overall

system. This is because the acquisition system, especially in tissue imaging, may include many sensors arranged in arrays where strong coupling exists not only between the array elements but also between the sensors and the surrounding structural components such as connectors, cables, container walls, and the object under test (in near-zone imaging). It is thus important to also have means of evaluating the PCS of the whole system, preferably through measurements.

Another benefit of this study is that it reveals the underlying physical reasons leading to higher sensitivities in the microwave imaging systems employing *S*-parameter measurements.

4.2 THEORY

In general terms, the sensitivity is the minimum input of a physical parameter that results in a detectable output.

4.2.1 Defining Sensitivity in Microwave Imaging

In microwave imaging, the output signals change in response to changes in the permittivity and the conductivity or, equivalently, the complex permittivity. For brevity, hereafter, we refer to the complex permittivity as permittivity.

In frequency-sweep measurements, the output signals are the *S*-parameters of the microwave network formed by the imaged object and the employed antennas. Therefore, here, a detectable output is a detectable change in the *S*-

parameters with respect to the baseline (or background) measurement.

The baseline measurement is that of the background—a medium the permittivity of which is assumed known. Thus, the physical-parameter input is a change in the permittivity with respect to that of the background. In imaging, however, the permittivity is a function of position. At each position, a sufficiently small volume can be defined (referred to as a *pixel* in 2-D imaging or a *voxel* in 3-D imaging) within which the permittivity is assumed constant. The voxel represents the smallest shape detail that can be captured in the image provided that it produces sufficiently strong signal. The voxel size is defined by the spatial resolution limit of the imaging technique, or, equivalently, by the width of its point-spread function at the half-power level.

Therefore, the definition of the physical-parameter input as a change in the permittivity must be confined to the volume of a single voxel. On the other hand, the size of the voxel is determined by the nature of the reconstruction algorithm and it should not influence the evaluation of the sensitivity of the acquisition hardware. In the case of small low-contrast targets, i.e., the case where the linear Born approximation holds [6], the scattered signals are proportional to the permittivity contrast and the volume of the target. Here, the contrast is defined as the difference between the target permittivity and that of the background. Thus, the smallest detectable change in the *S*-parameter is proportional to the voxel's volume, provided this volume is sufficiently small.

It is, therefore, appropriate to use the smallest detectable response change per unit volume.

Finally, to eliminate the dependence of the physical-parameter input on position, the assumption is made that the background is uniform.

To summarize, the physical contrast sensitivity (PCS) of a microwave system is defined here as the smallest permittivity change within unit volume in a known *uniform* background that results in a detectable change in the measured *S*-parameters. The smallest detectable change in the measured *S*-parameters can be defined through the standard deviation in the measurements of the background. Thus, the mathematical formulation of the above definition of the PCS is given by

$$\delta\varepsilon = \frac{\sigma(\boldsymbol{S}_{\mathrm{b}})}{|\,\partial S_{\mathrm{b}} / \partial\varepsilon\,|'} \tag{3.15}$$

where $\boldsymbol{S}_{\mathrm{b}}$ is the vector of a data set of N complex *S*-parameters acquired through multiple measurements of the background medium under the same conditions, $\sigma(\boldsymbol{S}_{\mathrm{b}})$ is the measurement uncertainty given by the standard deviation,

$$\sigma(\boldsymbol{S}_{\mathrm{b}}) = \sqrt{\frac{1}{N}\sum_{i=1}^{N} |\,S_{\mathrm{b},i} - S_{\mathrm{b,av}}\,|^2} \tag{3.16}$$

where

$$S_{\mathrm{b,av}} = \frac{1}{N}\sum_{i=1}^{N} S_{\mathrm{b},i} \tag{3.17}$$

and $|\partial S_{\mathrm{b}} / \partial \varepsilon|$ is the magnitude of the *S*-parameter derivative associated with the data set $\boldsymbol{S}_{\mathrm{b}}$. Further, $|\partial S_{\mathrm{b}} / \partial \varepsilon)|'$ is the derivative magnitude per unit volume, i.e.,

$$\left|\frac{\partial S_{\mathrm{b}}}{\delta \varepsilon}\right|' = \frac{|\partial S_{\mathrm{b}} / \partial \varepsilon|}{\delta V} \tag{3.18}$$

where δV is a known sufficiently small volume. The estimation of $|\partial S_{\mathrm{b}} / \partial \varepsilon|'$ is discussed in detail later.

We emphasize that all elements of a response set $\boldsymbol{S}_{\mathrm{b}}$ must represent the same measurement scenario, i.e., under ideal conditions, they are all the same. For example, $\boldsymbol{S}_{\mathrm{b}}$ may be comprised of the transmission coefficients measured with identical pairs of transmitting (Tx) and receiving (Rx) antennas separated by a given distance. However, $\boldsymbol{S}_{\mathrm{b}}$ may *not* be comprised of both transmission and reflection coefficients, or, of both co-pol and cross-pol responses, because such types of responses are not identical under ideal conditions.

In microwave imaging, unlike in device measurements, the *S*-parameter acquisition is extensive. It involves not only a frequency sweep but also a sweep over the acquisition surfaces enclosing the imaged volume (using mechanical scanning or switched arrays), switching between the transmitting

(Tx) antennas at a given position (e.g., to change the polarization of the incident field), switching between the receiving (Rx) antennas at a given position (e.g., to gather co-pol or cross-pol scattering data), etc. Thus, various sets of responses [see $\boldsymbol{S}_{\mathrm{b}}$ in (3.15)] are acquired depending on several factors: frequency, Tx position, Rx position, Tx antenna, Rx antenna, all of which may vary independently during data acquisition. Consequently, the PCS $\delta\epsilon$ depends on all of these factors as well.

To obtain a single measure of the hardware performance, we take the best (i.e., the smallest) $\delta\epsilon$ value across all employed orientations, positions and antennas.

Also, the PCS is a frequency-domain metric, i.e., it has a particular value at each frequency, since it is based on the measurements of the scattering parameters, which are frequency-domain responses. For wideband systems, such as those examined later, a single PCS value is obtained by averaging across the whole frequency band. In our validation examples, for comparison, the PCS is shown as a function of frequency in addition to the overall averaged estimate.

Finally, the PCS $\delta\epsilon$ is dependent on the electrical properties of the background medium, which is determined by the particular application. A PCS relative to the background permittivity ε_{b} may be a preferable metric since it provides the smallest detectable permittivity change per unit volume in

proportion to ε_b. This relative PCS is defined as

$$\delta\overline{\varepsilon} = \frac{\delta\varepsilon}{\varepsilon_b} = \frac{\sigma(S_b)}{\varepsilon_b \left| \partial S_b / \partial \varepsilon \right|'}. \tag{3.19}$$

In comparing the performance of measurement setups, a smaller PCS means better system performance, i.e., better sensitivity to variations of the spatial distribution of the permittivity in the examined volume. In addition, an estimate of $\delta\varepsilon$ (or $\delta\overline{\varepsilon}$) should be always accompanied by a description of the background electrical properties, especially when the background is lossy, because increased background losses result in weaker signals and worse sensitivity.

4.2.2 **Evaluation of the *S*-parameter Derivative**

The derivative $\partial S_b / \partial \varepsilon$ in (3.15) reflects the sensitivity of the *S*-parameter (in measurements of the background medium) with respect to the permittivity of a voxel located at a representative position $\mathbf{r}_c$ within the imaged volume. This position should be chosen so that it represents an averaged impact of a small target on all measured baseline responses. Hereafter, we refer to $\mathbf{r}_c$ as the scattering center. In a uniform background, $\mathbf{r}_c$ is simply the center of the imaged volume. The imaged volume is usually well defined by the acquisition surfaces enveloping it.

The derivative $\partial S_b / \partial \varepsilon$ can be estimated through electromagnetic (EM)

simulations of the background measurement scenario or directly through measurements. The simulation method is useful because it allows for the sensitivity estimation of a system or an antenna during the design stage. Also, it provides insight into the reasons leading to improved sensitivity. On the other hand, the measurement method is important for the evaluation of existing imaging systems and/or their antennas.

In order to obtain the minimum PCS $\delta\varepsilon$ for a given data set, we must select the maximum response sensitivity for this set; see (3.15). For a given response S_b, which corresponds to a selected Tx/Rx antenna pair (with its mutual distance and orientation fixed), the factors that influence its derivative are: (i) the distance from the scattering center $\mathbf{r}_c$ to the Tx antenna, (ii) the distance from $\mathbf{r}_c$ to the Rx antenna, (iii) the angular position of $\mathbf{r}_c$ with respect to the Tx antenna boresight, and (iv) the angular position of $\mathbf{r}_c$ with respect to the Rx antenna boresight. These factors may change when sampling over a surface, depending on the shape of the surface and the shape and orientation of the antennas. Therefore, to obtain its maximum value, the response sensitivity has to be explored for all possible placements of the selected Tx/Rx antenna pair relative to $\mathbf{r}_c$. This can be achieved by varying $\mathbf{r}_c$ while the Tx/Rx antenna is fixed (preferred in simulations) or by scanning the Tx/Rx antenna pair over the surface while $\mathbf{r}_c$ remains fixed (preferred in measurements).

4.2.2.1 ***S*-parameter derivative in simulations**

The general analytical sensitivity formula for the scattering parameters of microwave networks has been derived in [9]. When the parameter of interest is the complex permittivity of an object filled uniformly with an isotropic dielectric medium, the complex *S*-parameter derivative is computed as

$$\frac{\partial S_{jk}}{\partial \varepsilon} = \frac{i\omega}{2V_j^{\text{inc}} V_k^{\text{inc}}} \iiint_V \mathbf{E}_j \cdot \mathbf{E}_k dv \tag{3.20}$$

where V is the volume of the object, ε is its complex permittivity, ω is the radian frequency, $\mathbf{E}_\xi$ ($\xi = j,k$) is the electric field due to the excitation at port ξ, V_ξ^{inc} is the known modal magnitude of the incident wave at port ξ, and $i = \sqrt{-1}$. Bearing in mind the complex-permittivity representation $\varepsilon = \varepsilon' - i\varepsilon''$, the derivatives with respect to the real part ε' and the imaginary part ε'' are obtained from (3.18) as $\partial S_{jk} / \partial \varepsilon' = \partial S_{jk} / \partial \varepsilon$ and $\partial S_{jk} / \partial \varepsilon'' = -i \partial S_{jk} / \partial \varepsilon$, respectively.

For the purpose of calculating the PCS $\delta\varepsilon$ in (3.15), the volume V of the object of interest must be sufficiently small to represent a voxel, i.e., $V = \delta V$, so that the field distribution within δV is mostly uniform. Then, the *S*-parameter derivative per unit volume in the background medium with respect to the complex permittivity at $\mathbf{r}_c$ is calculated as

$$\left[\frac{\partial S_{\mathrm{b}}(\mathbf{r}_j,\mathbf{r}_k)}{\partial \varepsilon(\mathbf{r}_{\mathrm{c}})}\right]' = \frac{i\omega}{2V_j^{\mathrm{inc}}V_k^{\mathrm{inc}}}\mathbf{E}_j(\mathbf{r}_{\mathrm{c}})\cdot\mathbf{E}_k(\mathbf{r}_{\mathrm{c}}). \tag{3.21}$$

Here, the pair of position vectors $(\mathbf{r}_j,\mathbf{r}_k)$ describes the position of the Rx (j-th) and the Tx (k-th) antenna pair. The two field solutions $\mathbf{E}_\xi$ ($\xi = j,k$) in (3.21) are obtained by simulating the whole structure (antennas and background medium) by exciting port j or port k, respectively, regardless of whether this port is connected to a Tx or an Rx antenna in the actual setup. If S_{b} is a reflection coefficient, i.e., $j=k$, one simulation is needed with the j-th port excited. Conversely, if S_{b} is a transmission coefficient, two simulations are needed, where ports j and k are excited, one at a time. In general, for a network of K ports, in order to obtain the derivatives of all *S*-parameters S_{jk}, $j,k=1,\ldots,K$, K simulations need to be carried out to obtain the K field distributions.

From (3.21), it is clear that the maximum derivative is obtained when the maximum value of the field product $|\mathbf{E}_j\cdot\mathbf{E}_k|$ is achieved at the scattering center $\mathbf{r}_{\mathrm{c}}$ for a particular placement of the k-th and j-th antennas. What matters is the *mutual* placement of $\mathbf{r}_{\mathrm{c}}$ and the antenna pair. When the acquisition surface is symmetric (e.g., planar, cylindrical, or spherical), there is no need to vary the antenna placement in the simulations. It is far more

efficient to vary $\mathbf{r}_c$ because the simulations provide the field distribution in the whole computational volume, i.e., at all possible positions relative to the Tx/Rx antenna pair. Thus calculating the derivative in (3.21) can be efficiently done for all mutual placements defined by $(\mathbf{r}_j, \mathbf{r}_k)$ and $\mathbf{r}_c$.

Any high-frequency simulator can be used to obtain the field distributions in (3.21), provided that it offers utilities to export the field solution at user-defined locations and frequencies. Most commercial solvers have such utilities.

Also, some commercial software packages provide accurate *S*-parameter derivatives at very low computational cost, including derivatives with respect to the real and imaginary parts of the permittivity of objects [18], [11]. This capability is referred to as *exact* or *adjoint S*-parameter sensitivity analysis. If such software is used to obtain the *S*-parameter derivatives, virtual objects of sufficiently small volume δV (typically spheres or cubes) have to be defined at all desired locations in the background region and their permittivity must be submitted as parameters for sensitivity analysis. The resulting *S*-parameter derivatives must then be divided by the volume δV in order to obtain $|\partial S_b / \partial \varepsilon|'$; see (3.18).

Finally, it should be noted that while the derivative in (3.15) can be estimated through simulations, the PCS calculation still requires the measurement uncertainty, which is established experimentally.

4.2.2.2 ***S*-parameter derivative in measurement**

The *S*-parameter acquisition in imaging involves scanning the antennas over the acquisition surfaces enveloping the imaged volume. Alternatively, electronically switched arrays may be used to sample the baseline signals at these surfaces. In both cases, two acquisitions need to be made to obtain an estimate of the *S*-parameter derivative: with and without a weak scatterer at $\mathbf{r}_c$ in the background medium.

The *S*-parameter derivative (per unit volume) is estimated using a finite-difference approximation where the difference between the two signals, with and without a scatterer, is divided by the known permittivity contrast of the scatterer:

$$\left[\frac{\partial S_b(\mathbf{r}_j,\mathbf{r}_k)}{\partial \varepsilon(\mathbf{r}_c)}\right]' \approx \frac{1}{\delta V}\cdot\frac{\Delta S(\mathbf{r}_j,\mathbf{r}_k)}{\Delta \varepsilon(\mathbf{r}_c)} = \frac{1}{\delta V}\left[\frac{S_s(\mathbf{r}_j,\mathbf{r}_k)-S_{b,av}}{\varepsilon_s(\mathbf{r}_c)-\varepsilon_b}\right]. \qquad (3.22)$$

Here, $S_s(\mathbf{r}_j,\mathbf{r}_k)$ is the *S*-parameter acquired (with the scatterer in place) at the Rx/Tx locations given by $(\mathbf{r}_j,\mathbf{r}_k)$, ε_b and ε_s are the known permittivities of the background and the scatterer, respectively, and δV is the known volume of the scatterer. The maximum derivative is selected among the set obtained at all locations $(\mathbf{r}_j,\mathbf{r}_k)$ and is then used in (3.15). For best results, several measurements (scans) should be taken with the scatterer in place, and, an average should be taken of all values obtained through (3.22).

Note that the target contrast $\Delta\varepsilon$ must be large enough to provide a response difference ΔS which is sufficiently larger than the measurement uncertainty σ. If $\Delta S \le \sigma$, the PCS estimate is not valid. On the other hand, the scatterer must be sufficiently weak so that its contrast and size satisfy the constraints associated with the linear Born approximation [6]:

$$\left|k_{\mathrm{b}} L(\varepsilon_{\mathrm{s}} - \varepsilon_{\mathrm{b}}) / \varepsilon_{\mathrm{b}}\right| \ll 1. \tag{3.23}$$

Here, k_{b} is the background wave number and L is the largest dimension of the scatterer.

4.2.2.3 **The Smallest Detectable Change**

Once the PCS $\delta\varepsilon$ is obtained from (3.15), either the smallest detectable permittivity contrast for a given target size or the smallest detectable size for a given target contrast can be determined from the relationship

$$\delta\varepsilon = \Delta\varepsilon \cdot \Delta V \tag{3.24}$$

where $\Delta\varepsilon$ is the minimum detectable permittivity contrast for a target of size ΔV or, alternatively, ΔV is the minimum detectable volume for a target of contrast $\Delta\varepsilon$. In both cases, the estimation is valid only if the contrast and the size fulfill the constraint (3.23).

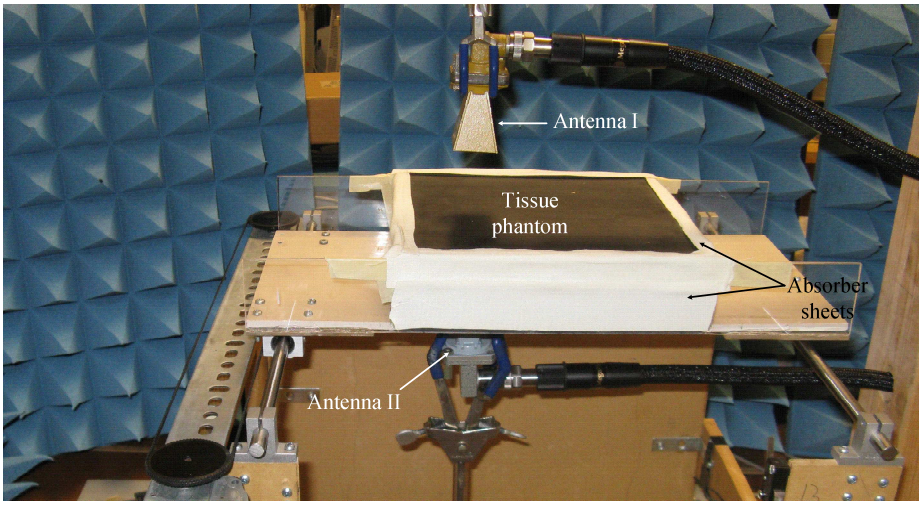

Fig. 4.2-1. Photo of the planar raster scanning setup

4.3 VALIDATION

The proposed method is validated through the sensitivity estimation of a planar raster scanning imaging setup that is being used in experiments with tissue samples and phantoms.

4.3.1 **Planar Raster Scanning Setup and Antenna Description**

In planar raster scanning, two antennas (or switched antenna arrays), are facing each other along boresight and are moving together to scan two parallel planes on both sides of the imaged volume. Fig. 4.2-1 shows the photograph of the scanning setup used here, which employs two antennas, one transmitting and one receiving. Four different antennas are being used in the examples as described later.

Fig. 4.2-1 also shows a tissue phantom and dielectric substrate (Taconic

CER-10; $\varepsilon_r = 10, \tan\delta \approx 0.0035$) underneath the phantom to hold it. The measurements with a vector network analyzer (VNA) Agilent-E8363B produce the *S*-parameters of a two-port network, both the reflection and transmission coefficients, as functions of x and y, which define the sampling position. Note that in this setup the antennas are fixed. It is the phantom which is being moved relative to the antennas by the scanning table using two stepper motors. The scanned area of this system can extend up to 18 cm along x and y and the user-defined sampling step can be anywhere between 1 mm and 10 mm.

In the all examples, the background medium (baseline phantom) is a 3 cm thick dielectric slab of lateral size 20 cm by 20 cm. Four absorber sheets, each of thickness 8 mm, are placed around the phantom edges (see absorbing sheets covered by white paper tape in Fig. 4.2-1) to reduce interference and to suppress waves propagating along the phantom-air interface. The overall scanned area is 8 cm by 8 cm with a sampling interval of 1 mm. The frequency range is from 3 GHz to 10 GHz with 101 sampling points. The resolution bandwidth (RBW) of the VNA is set to 10 kHz; unless specified theraise; the averaging factor is 10. The power level at the Tx antenna port is 8 dBm.

To model the background tissue phantom in simulations, the phantom's constitutive parameters are extracted by solving a least-square problem in HFSS ver. 13 [18] using sequential nonlinear programming optimizer. The least-square problem is solved to match the measured and the simulated

magnitude of the transmission coefficient $|S_{12}|$ when the 1st antenna set is used. The real part of the extracted relative permittivity is mostly constant in the whole frequency range and has an average value of 9.13. The loss tangent, however, exhibits significant dispersion. It is plotted versus frequency in Fig. 4.3-1.

In the first example, two identical antennas are used on both sides of the planar scanning setup. They employ an ultra-wideband (UWB) design for the frequency range from 3 GHz to 10 GHz. The design consists of a TEM horn and a UWB impedance matching structure with a coaxial feed, all of which are embedded in a solid dielectric medium [1]. These antennas are being used in experiments on breast-tissue phantoms as well as on animal tissue samples. Hereafter, this antenna pair is referred as the 1st antenna set.

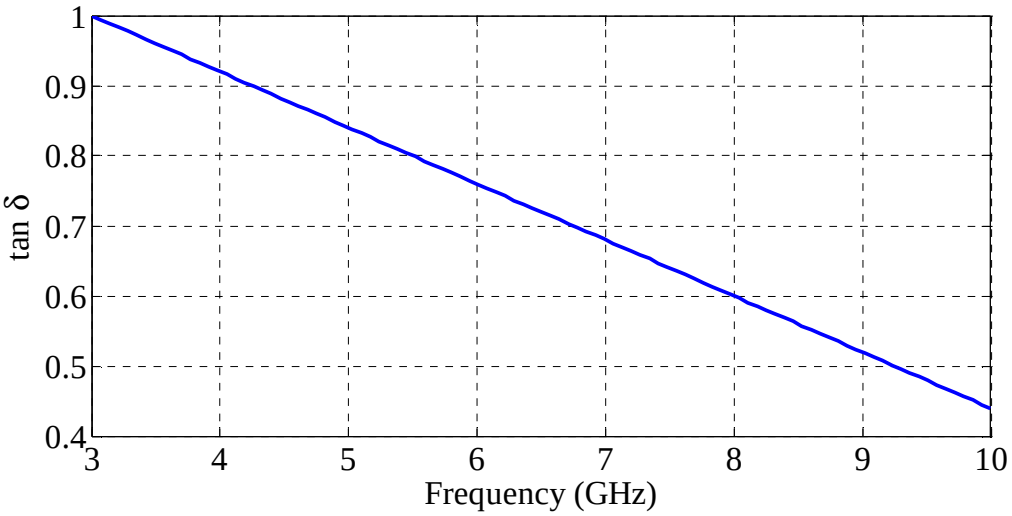

Fig. 4.3-1. The phantom's extracted loss tangent.

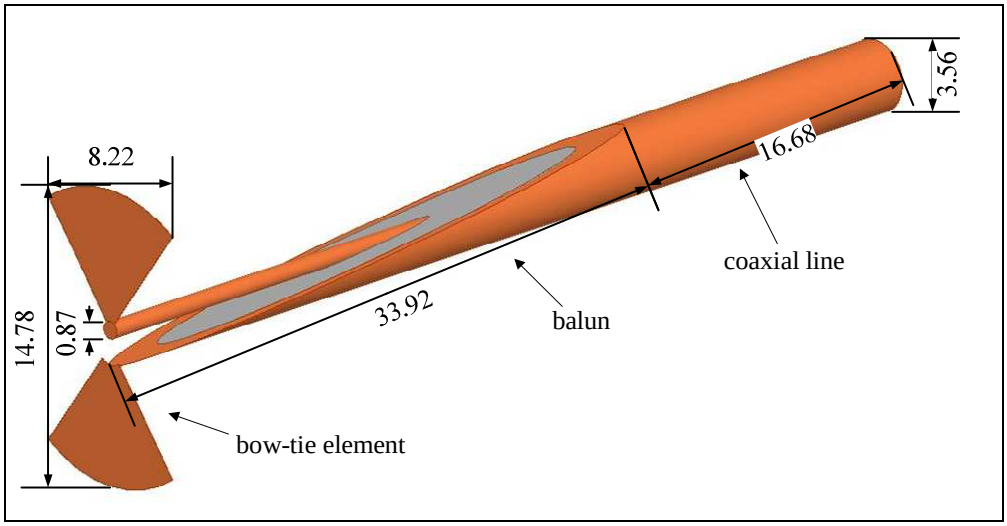

Fig. 4.3-2. Bow-tie antenna structure with tapered balun.

In the second example, a different set of two identical antennas (introduced in chapter 2 and reported in [13]) is investigated with the same scanning setup. These antennas also exploit a UWB TEM horn design but feature different feed structure (a tapered coaxial balun) and improved shielding compared to the 1st antenna set. We refer to this antenna pair as the 2nd antenna set.

In the third example, a set of two broadband bow-tie antennas is investigated. This design has not been published and is briefly described here [1]. Fig. 4.3-2 shows the inner structure and the dimensions of the bow-tie radiating element together with its tapered coaxial balun. The bow-tie element is printed on one side of a *Rogers 4003* printed circuit board (PCB) of

[1] The bow-tie antennas were designed in Computational Electromagnetic Research Laboratory at McMaster University by Ali Khalatpour and fabricated by Justin McCombe.

thickness 0.02" (0.508 mm) of permittivity ε_r = 3.38 and dielectric loss tangent tanδ = 0.0027. The bow-tie element faces the measured tissue phantom, while the back of the PCB (not metalized) is glued to a solid dielectric medium of ε_r = 9 and tanδ = 0.005. The feeding balun is embedded in the solid dielectric. The bow-tie is used in a switched array structure consisting of nine elements. Fig. 4.3-3 shows the bow-tie array. Two sets of identical arrays as are used here. The sensitivity is evaluated for the pair of the central elements (see element 1 in Fig. 4.3-3). This pair is the most sensitive to permittivity variations centered along the array boresight. We refer to this antenna pair as the 3rd antenna set.

In the fourth example, a quad-ridge horn antenna [14] is used as a Tx antenna while the bow-tie element acts as a sensor. The quad-ridge horn is a dual-polarization (two-port) antenna designed for tissue illumination through direct contact, i.e., without a coupling medium. Therefore, for better impedance match with the tissue medium, the quad-ridge structure is embedded in a solid dielectric medium, similarly to the TEM horn designs described above. For best sensitivity, the Tx polarization is aligned with that of the receiving bow-tie. We refer to this antenna pair as the 4rd antenna set.

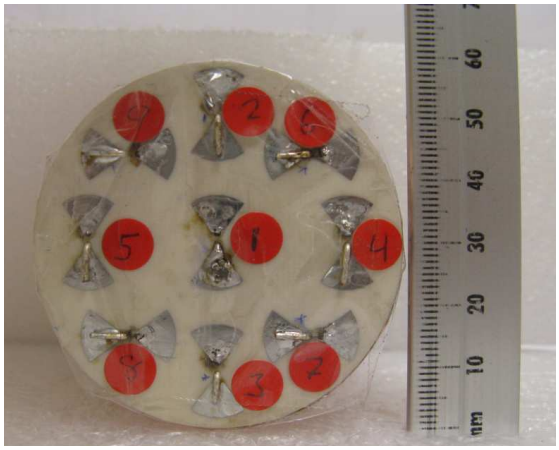

(a)

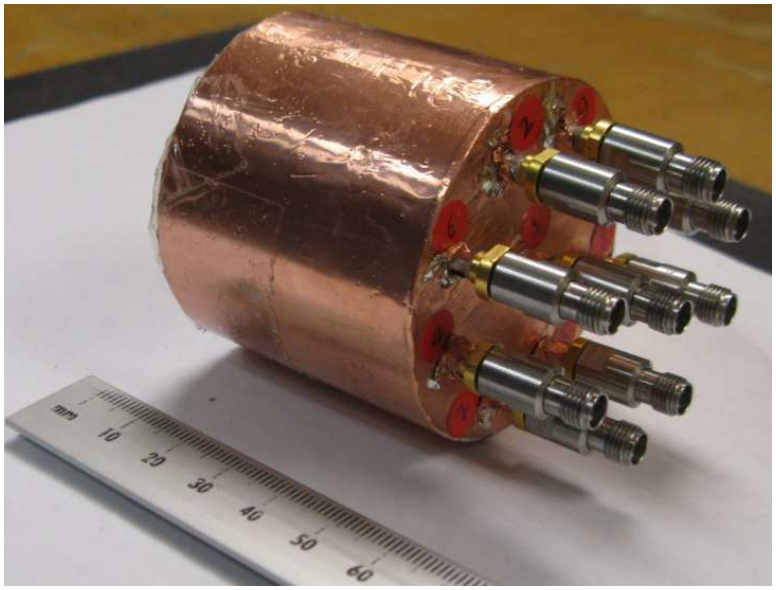

(b)

Fig. 4.3-3. Fabricated bow-tie array: (a) front surface (facing the tissue phantom), and (b) back view showing the coaxial connectors.

To illustrate the level of alignment between simulation and measurement achieved by the phantom-property extraction,

Fig. 4.3-4 shows the measured and the simulated $|S_{12}|$ in the case of the

baseline data acquisition (background phantom). The plots show the $|S_{12}|$ transmission coefficient for both antenna sets. The agreement between the simulated and measured responses is good for the 1st antenna set. The comparison for the 2nd antenna set shows significant discrepancies at frequencies below 5 GHz. These discrepancies are mostly due to the fabrication inaccuracies of the tapered coaxial balun in combination with the response being very sensitive to these inaccuracies. As this low-frequency misalignment has nothing to do with the phantom electrical properties, it cannot be compensated for by the phantom-property extraction.

There are various strategies that could be pursued to further improve the alignment of simulations and measurements; however, such investigations are irrelevant here. Such discrepancies are not uncommon in near-field data acquisition scenarios where complex antenna structures, uncertainties in the material parameters, positioning errors, radiation leakage and imperfect isolation make for an involved, often intractable, reasons for discrepancies between simulations and measurements. Additionally, tissue phantoms exhibit high loss resulting in very weak responses, the level of which is often comparable to the numerical accuracy of the simulation. For example, the mesh convergence error used here is set to 0.005 and, as evident from

Fig. 4.3-4, the signal levels are at or below this value

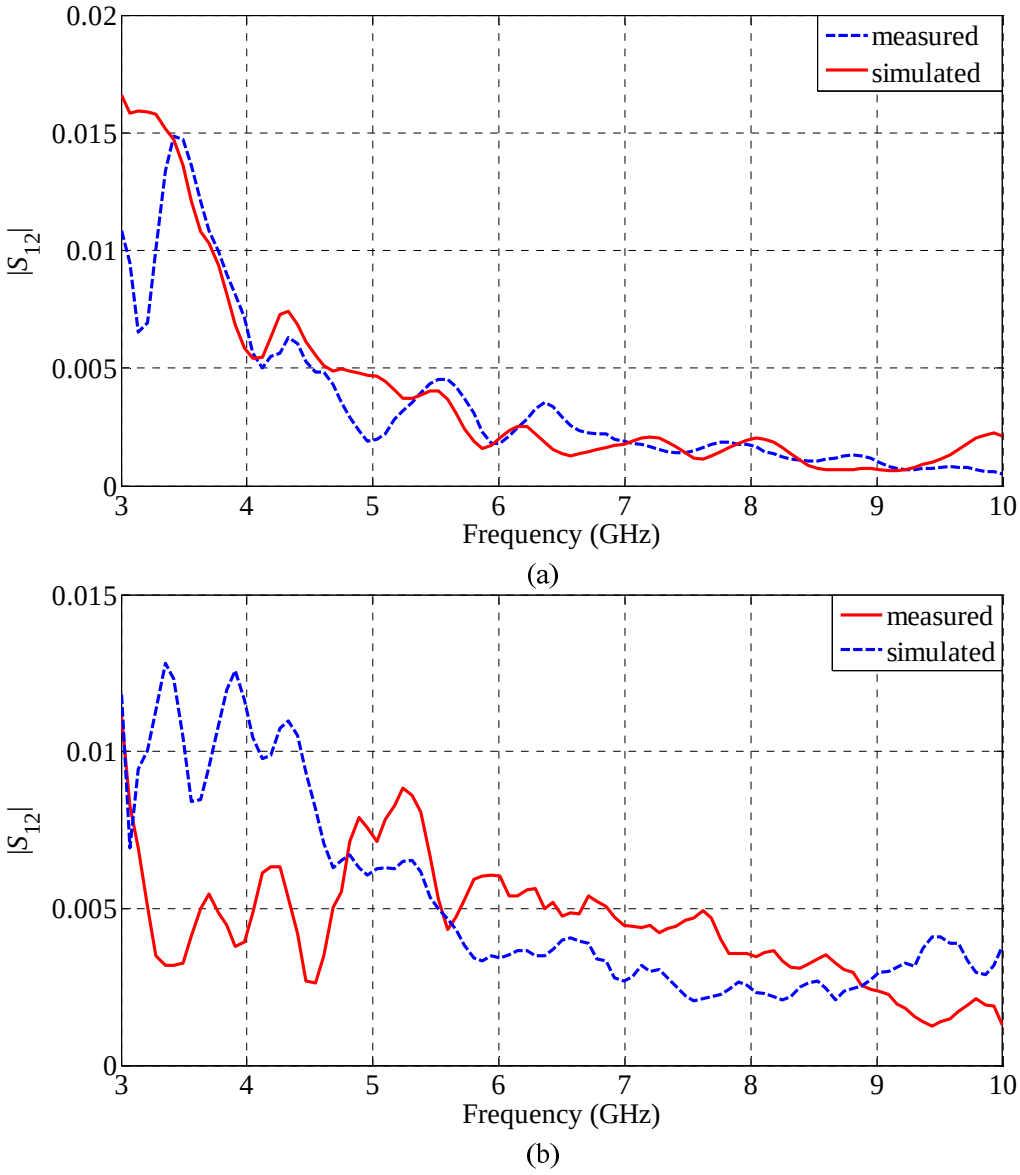

Fig. 4.3-4. Comparison of the baseline measured and simulated $|S_{12}|$ of the scanning system when the Tx/Rx pair employs: (a) the 1st antenna set, and (b) the 2nd antenna set.

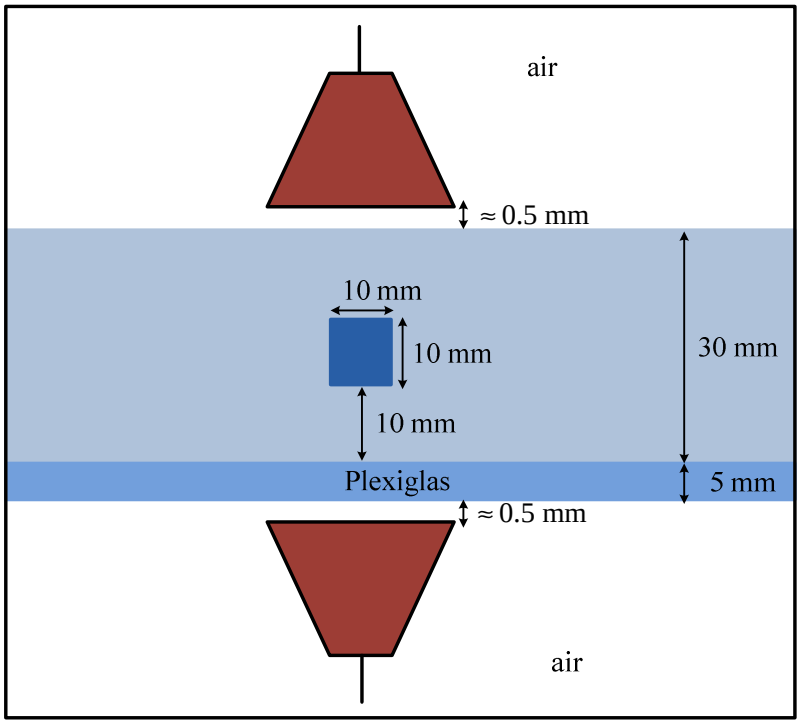

Fig. 4.3-5. Schematic of the raster scanning setup showing the air gap, the *plexiglas* plate holding the phantom, the phantom layer, and the small scatter target.

In addition to the baseline measurements, we also need to perform measurements on a small scattering target embedded at the center of the background phantom. The target is a ceramic cylinder of radius 10 mm and height 10 mm (see Fig. 4.3-5). Its relative permittivity is $\varepsilon_r = 12$ and its loss tangent is $\tan\delta = 0.0013$.

Fig. 4.3-5 also shows other details describing the raster scanning setup such as the air gap between the antenna face and the tissue phantom as well as the thickness of the *Plexiglas* plate.

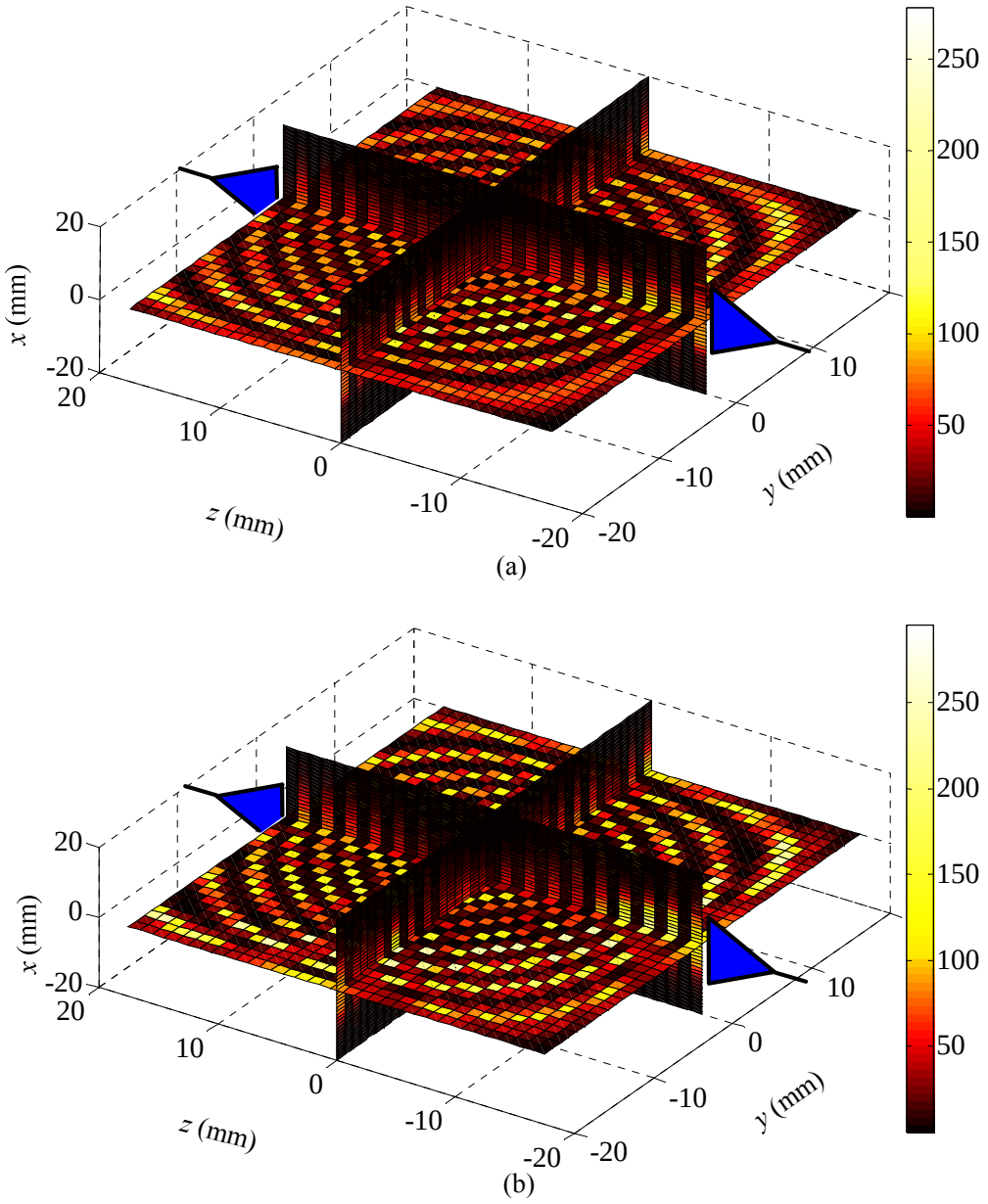

Fig. 4.3-6. *S*-parameter derivative per unit voxel as a function of the voxel position obtained in simulations with the 1st antenna set: (a) 6 GHz, (b) 8 GHz.

4.3.2 *S*-parameter Derivatives: Simulation vs. Measurement

To estimate the PCS, the *S*-parameter derivatives per unit volume are needed; see (3.15). For the simulation-based derivative estimation, the commercial software HFSS ver. 13 [18] is used to perform an *S*-parameter frequency sweep from 3 GHz to 10 GHz with 101 samples. The mesh convergence error for the *S*-parameters is set to 0.005. The absorbing sheets wrapped round the sides of the tissue phantom are modeled with radiation boundary conditions since their electrical properties are not available. The antennas are modeled with as much detail as possible, including the baluns and the coaxial ports. The coaxial connectors, however, are not included in the simulation due to the excessive computational requirements of the entire model.

As explained in section 4.2.2.1, in the simulation model, the antennas are at a fixed position. The *S*-parameter derivative is calculated with the sensitivity formula (3.21) as a function of position, $\mathbf{r}_c$ in (3.21), and the result is averaged over a volume of $\pi/4$ cm^3 at each position. This volume corresponds to the actual small scatterer used in the measurements. The E-field distributions are exported on a uniform 3-D grid of 1 mm spacing using the *Field Calculator* tool in the post-processing module of HFSS. To obtain $|\partial S_b / \partial \varepsilon|'$, the maximum derivative is selected among all values corresponding to all

positions $\mathbf{r}_c$ within the phantom. Since the measurements employ a small scatterer at the center of the background phantom, for the sake of comparison, here, $\mathbf{r}_c$ is restricted to the phantom's mid-plane.

The simulations also reveal that the *S*-parameter derivatives vary substantially with the position of the voxel. This behavior is dictated by their relationship with the field distribution, see (3.21). Nonetheless, the maximum derivative value is always correlated with the directions of the maximum radiation of the two antennas because stronger field values translate into larger derivatives as (3.21) suggests. Fig. 4.3-6 illustrates this behavior in the case of antenna set 1 at

6 GHz and at 8 GHz. The antennas are polarized along *x*. The plots show the derivative magnitude at the respective frequency calculated at each voxel (of volume $\pi/4$ cm^3) and plotted in three mutually orthogonal planes. It is evident that it varies with position significantly and has a distinct "interference" pattern. This is due to the maxima and the minima of the dot product of the two fields (the one due to the *j*-th antenna and the one due to the *k*-th antenna). The figure also shows how these distributions change with frequency where a shorter wavelength (that at 8 GHz compared to the one at 6 GHz) implies a denser pattern of minima and maxima. Furthermore, as the medium is very lossy, the field strength and, as a consequence, the magnitude

of the response derivative attenuate quickly. This is particularly pronounced in the vertical direction in which the antenna has a relatively narrow beam. Also, due to the fact that the two TEM horns are aligned along each other's boresight, the dot product of their respective fields is the strongest in the *zy* plane.

The measurements are performed with the planar raster scanning setup described in section 4.3.1. The *S*-parameters are acquired as functions of the sampling position (x, y) with both phantoms: (a) the background phantom, and (b) the target phantom which is the same as the background phantom except that it contains a small scatterer at its center (see Fig. 4.3-5). The small scatterer is a ceramic cylinder of height 10 mm, diameter 10 mm, relative permittivity $\varepsilon_r = 12$ and loss tangent $\tan\delta$ = 0.0013. The electrical properties of this scatterer are constant in the whole frequency band. The derivative (also a function of the sampling position) is evaluated using the finite-difference approximation (3.22). Then, the maximum derivative magnitude $|\partial S_{\mathrm{b}} / \partial \varepsilon|'$ is selected.

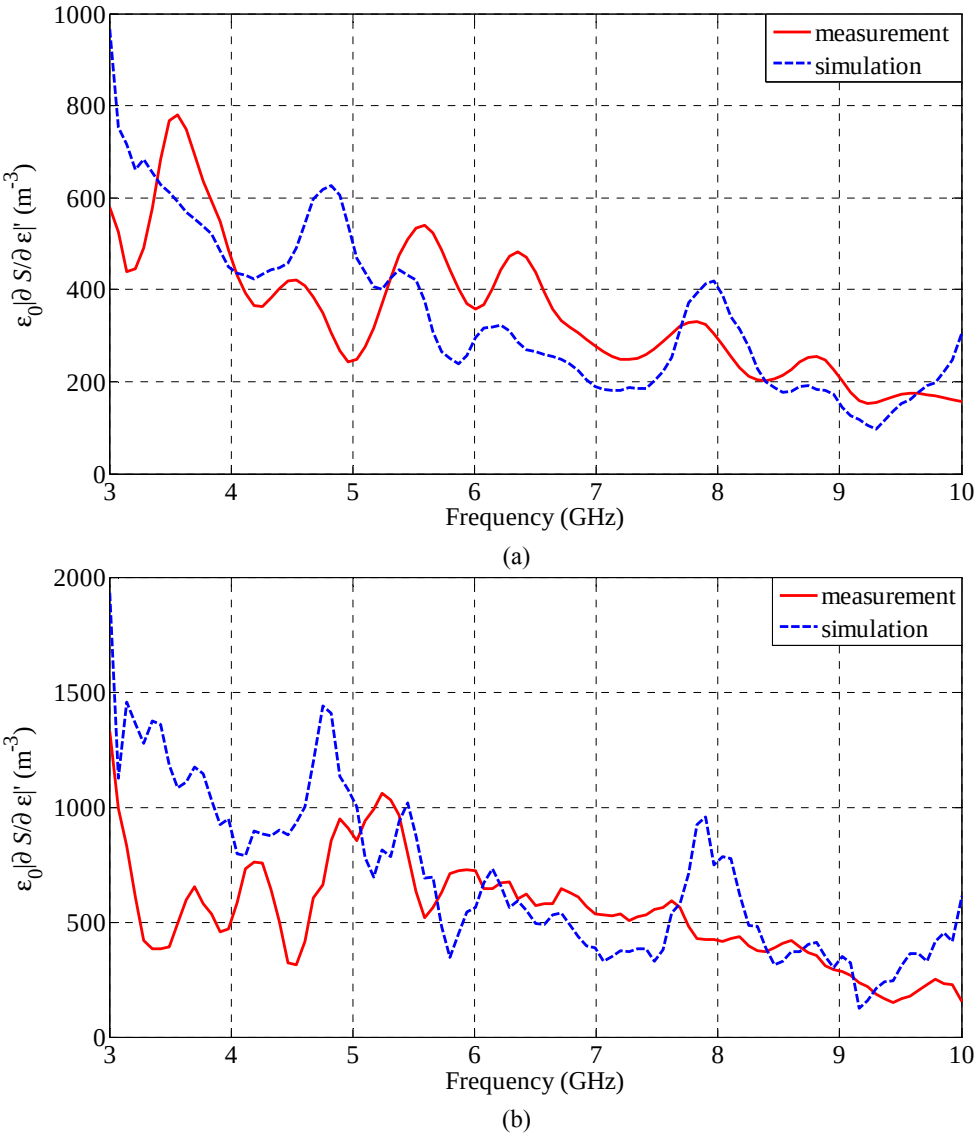

Fig. 4.3-7. *S*-parameters derivative values per unit volume evaluated via the simulation approach explained in section 4.2.2.1 and the measurement approach explained in section 4.2.2.2 for the raster scanning imaging setup with TEM horn antennas introduced in (a) [1] and, (b) [13].

The derivative results from the simulations and the measurements for the 1st and the 2st antenna sets are shown in Fig. 4.3-7 a) and b), respectively. Fairly

good agreement is observed for most of the frequency range. As expected, the only significant discrepancy between simulations and measurements occurs for antenna set 2 below 5 GHz. As explained in Section 4.3.1, this discrepancy exists for the *S*-parameters themselves and it is expected to affect the *S*-parameter derivatives as well.

4.3.3 **PCS Evaluation**

Once the *S*-parameters derivatives per unit volume are available, the PCS is evaluated using (3.15). The measurement uncertainties are evaluated with the standard deviation in (3.17) from the baseline measurements at each frequency. The PCS has been evaluated for the four antenna sets described in Section 4.3.1. Fig. 4.3-8 shows their normalized PCS values, see (3.19), versus frequency. The results suggest that the two horn-antenna sets perform similarly across the frequency band. The set of bow-tie antennas has the worst PCS on average. Its weak performance is due to the lower directivity and radiation efficiency compared to the horn antennas. The 4^{th} antenna set, which employs a quad-ridge horn as a Tx antenna and the bow-tie element as the Rx antenna, performs very well at higher frequency where its directivity is relatively high. This behavior illustrates the importance of the Tx antenna ability to provide strong illuminating fields in addition to the performance of the sensor (Rx antenna).

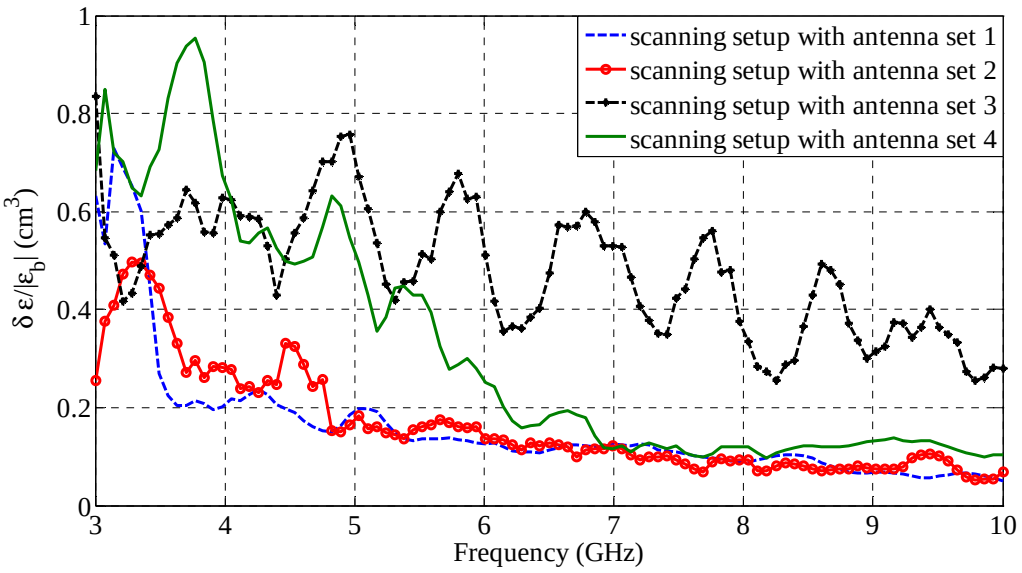

Fig. 4.3-8. Normalized PCS versus frequency for the raster scanning setup with antenna sets 1 and 2.

As discussed before, from the PCS, the minimum detectable volume for a given target contrast can be evaluated from (3.24). Alternatively, the minimum detectable permittivity contrast for a given size can also be estimated. For example, for an object of 1 cm^3 volume, the minimum detectable normalized contrast ($\Delta\varepsilon/|\varepsilon_b|$), averaged over all frequencies, is 0.1613 and 0.1646 with antenna sets 1 and 2, respectively. Thus, the two antenna sets perform very similarly being capable of detecting a relative as low a contrast as 16 % for the given background of thickness 3 cm, $\varepsilon_r \approx 9.13$ and loss tangent as shown in Fig. 4.3-1. In comparison, the average normalized PCS value for the 3rd antenna set is 0.4746. Therefore, the bowtie antennas need at least 47% relative

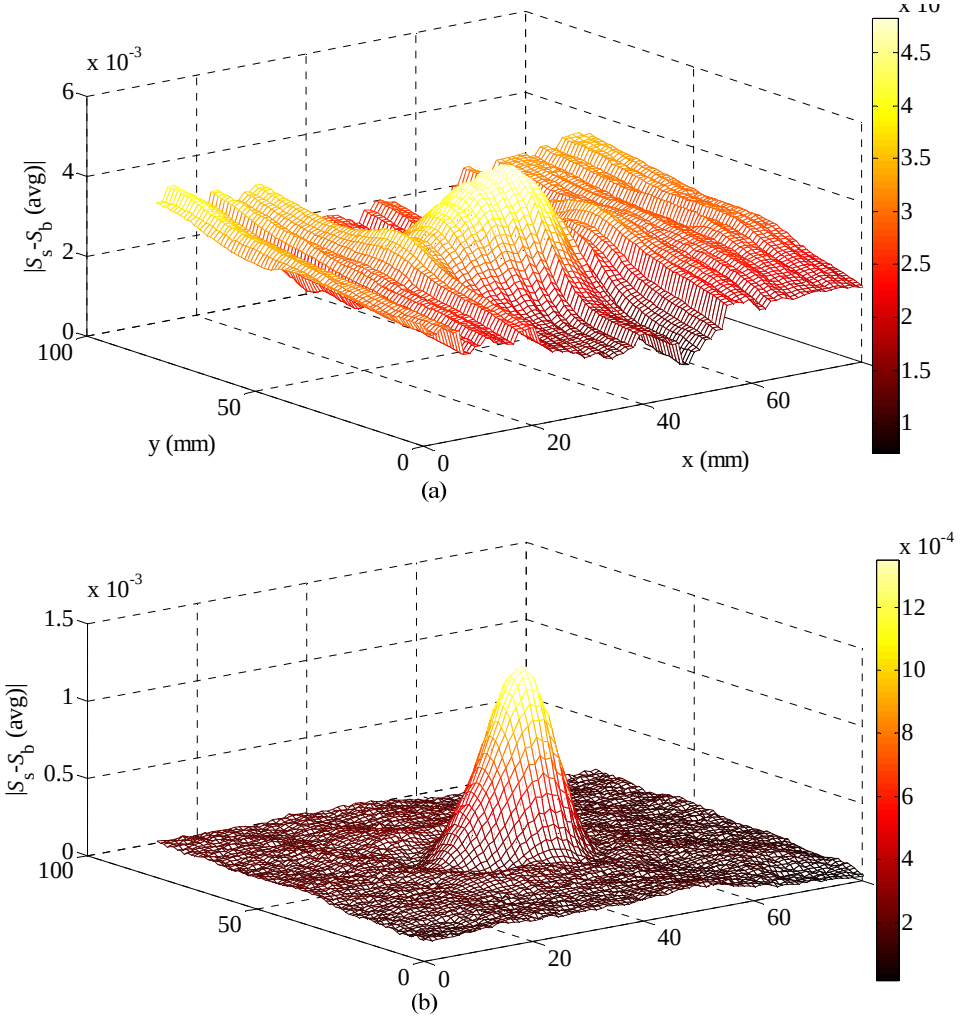

Fig. 4.3-9. Difference between the transmission coefficients measured with and without the small scatterer in the raster scanning setup with the 1st antenna set at: (a) 3 GHz, and (b) 5 GHz.

contrast for the same background to detect the 1 cm^3 scatterer. This value is 32% for the 4th antenna set.

Fig. 4.3-9 provides a different illustration of the performance of the raster scanning setup with the 1st antenna set. The plot shows the *xy* dependence of the magnitude of the difference of the complex transmission coefficients with

and without the small scatterer used in the *S*-parameter derivative estimation through measurement. This difference is essentially the signal due to the scatterer. The two plots show the *xy* dependence of this signal at 3 GHz and at 5 GHz. These two frequencies are chosen based on the results in Fig. 4.3-8 where we observe that the relative PCS is relatively large (or bad) at 3 GHz and is significantly smaller (or better) at 5 GHz. Therefore, these two very different values correlate with the respective plots of the transmission coefficients in terms of the clarity with which they show the target signature. It is evident that the setup has better detection performance at 5 GHz, which is in agreement with the PCS frequency dependence shown in Fig. 4.3-8.

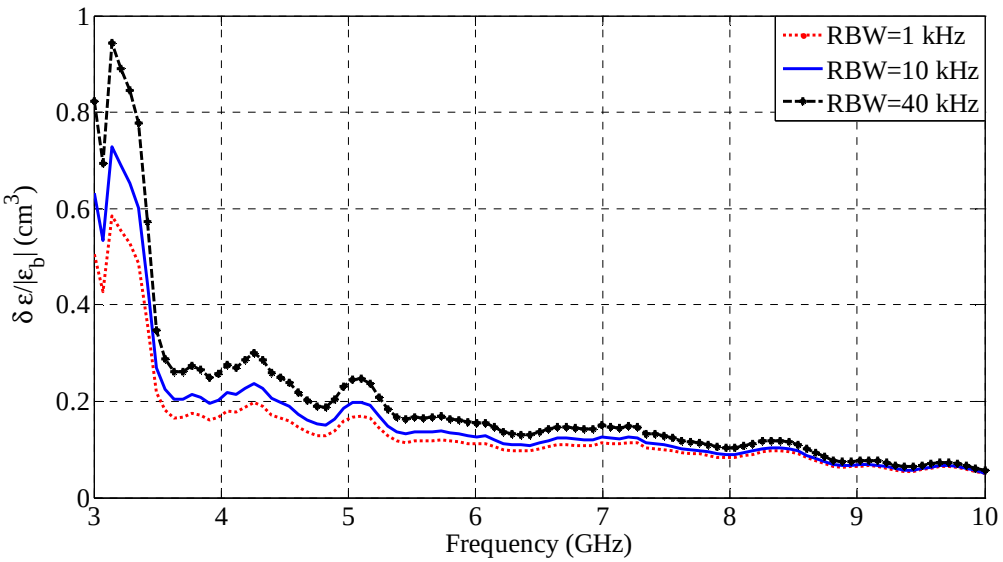

Fig. 4.3-10. Illustration of the effect of the VNA resolution bandwidth (RBW) on the PCS of the raster-scanning setup with the 1st antenna set.

One of the important factors that can affect the PCS of the microwave imaging system is the resolution bandwidth (RBW) of the VNA. The impact of the RBW varies depending on how the instrument noise compares with the external noise in the measurement environment and the level of the uncertainties due to positioning errors, spurious signals due to radiation leakage, temperature variations, etc. Fig. 4.3-11. shows the effect of the VNA RBW on the normalized PCS of the raster scanning setup with the 1st antennas set. As expected, a larger RBW leads to higher thermal noise levels and thus a higher (or worse) PCS. The impact of the RBW on the PCS is less significant at high frequencies because at these frequencies the uncertainties due to the external factors, such as positioning errors and leakage, dominate. Decreasing the instrument's RBW has no influence on such factors.

4.4 CONCLUSION

The PCS of microwave imaging systems employing scattering-parameter measurements is defined and a method to evaluate it is proposed. For the system under evaluation, the PCS estimates the smallest detectable target contrast for a given size or *vice versa*. The definition relies on the evaluation of the *S*-parameters derivatives, for which measurement-based and simulation-based methods are proposed. Validation and illustration of the PCS evaluation methodology is carried out for a raster-scanning imaging system where four

different antenna arrangements are used. The proposed methodology provides common means to quantify and compare the sensitivity performance of microwave systems used in tissue imaging as well as the antennas used as sensors.

4.5 REFERENCES

[1] R. F. Wagner and D. G. Brown, “Unified SNR analysis of medical imaging systems,” *Phys. Med. Biol*., vol. 30, pp. 489–518, 1985.

[2] R. F. Wagner, M. F. Insana, and D. G. Brown, “Statistical properties of radio-frequency and envelope-detected signals with applications to medical ultrasound,” *J. Opt. Soc. Am. A*., vol. 4, no. 5, pp. 910–922, 1987.

[3] D. L. Parker, Y. P. Du, and W. L. Davis, “The voxel sensitivity function in Fourier transform imaging: applications to magnetic resonance angiography.” *Mag. Res. Med*. vol, 33, no. 2, pp. 156–162, 1995.

[4] C. G. Graff, and K. J. Myers, “The ideal observer objective assessment metric for Magnetic Resonance Imaging,” *In Information Processing in Medical Imaging*, pp. 760–771, Berlin: Springer, 2011.

[5] N. Q. Nguyen, C. K. Abbey, and M. F. Insana, “Objective assessment of sonographic quality I. Task information,” *IEEE Trans. Med. Imag*., vol. 32, no. 4, pp. 683–690, Apr. 2013.

[6] W. C. Chew, *Waves and Fields in Inhomogeneous Media*. New York: IEEE Press, 1995.

[7] P. M. Meaney, M. W. Fanning, R. M. di Florio-Alexander, P. A. Kaufman, S. D. Geimer, T. Zhou and K. D. Paulsen. "Microwave tomography in the context of complex breast cancer imaging," *Conf. Proc. IEEE Eng. Med. Biol*. Soc., pp. 3398–3401, 2010.

[8] M. Klemm, J. A. Leendertz, D. Gibbins, I. J. Craddock, A. Preece, and R. Benjamin, "Microwave radar-based differential breast cancer imaging: imaging in homogeneous breast phantoms and low contrast scenarios," *IEEE Trans. Antennas Propag*., vol. 58, no. 7, pp. 2337–2344, July 2010.

[9] M.S. Dadash, N.K. Nikolova, and J.W. Bandler, "Analytical adjoint sensitivity formula for the scattering parameters of metallic structures," *IEEE Trans. Microw. Theory Techn*., vol. 60, no. 9, pp. 2713–2722, Sep. 2012.

[10] Matlab7.1 ed. Natick, MA, The MathWorks, Inc., 2005.

[11] Ansoft Corporation [Online]. Available: http://www.ansoft.com

[12] Computer Simulation Technology [Online]. Avaible https://www.cst.com/

[13] R. K. Amineh, M. Ravan, A. Trehan, and N. K. Nikolova, "Near-field microwave imaging based on aperture raster scanning with TEM horn

antennas," *IEEE Trans. Antennas Propag*., vol. 59, no. 3, pp. 928−940, Mar. 2011.

[14] K. Moussakhani, R.K. Amineh, and N.K. Nikolova, "High-efficiency TEM horn antenna for ultra-wide band microwave tissue imaging," *IEEE AP-S/URSI Int. Symp. on Antennas Propag*, July 2011.

[15] M.S. Dadash, K. Moussakhani, and J.J. McCombe, "Quad-ridge horn antenna for tissue measurements," *Computational Electromagnetics Res. Lab., McMaster University, CEM-R-69*, June 2014.

Chapter 6

Conclusion

In this thesis, various metrics of the hardware performance of the microwave imaging systems is investigated. Also, methods to estimate the efficiency and the sensitivity of the microwave imaging systems and their components have been introduced and applied in practical scenarios.

A new UWB TEM horn antenna is proposed for microwave tissue imaging. The new antenna has several advantages over the previously proposed UWB TEM horn antenna in terms of coupling efficiency and immunity to electromagnetic interferences. These characteristics lead to the better dynamic range of the microwave imaging setup. Moreover, the sensitivity of the imaging setup is increased, which enables the detection of smaller tumor simulants in thicker phantoms.

The proposed measurement-based method for evaluating the efficiency of antennas can be used for antennas operating in a complex (layered, lossy, dispersive) medium and in a single or a wide bandwidth frequency. The sensor efficiency and dynamic range of measurement setup are not the only factors affecting the sensitivity of the acquisition hardware. PCS can be used to compare the whole microwave system in terms of their sensitivity in detecting a tumor. It provides a quantitative approach to compare the acquisition hardware of microwave imaging systems using *S*-parameters measurements. For the system under evaluation, the PCS estimates the smallest detectable target contrast for a given size or *vice versa*. The proposed methodology provides common means to quantify and compare the sensitivity performance of microwave systems used in tissue imaging as well as the antennas used as sensors in microwave imaging.

From the experience gained during the course of this work, the author suggests the following research topics to be addressed in future developments.

- To increase the dynamic range of microwave imaging system, further efforts toward decreasing the electronic and mechanical noise in the microwave system are needed. Substantial improvement in this respect can be achieved if the mechanically scanned antennas are replaced by electronically switched arrays. This will eliminate the uncertainties

associated with the mechanical antenna positing. Also the predictability of the acquisition environment should be improved by better shielding and isolation.

- The physical sensitivity method can be used in the design stage of the microwave imaging system to increase the sensitivity of the system. Especially, PCS can be useful in designing of beam steering arrays for MWI.
- The physical sensitivity method uses frequency domain measurements. This method can be extended to time domain measurements.

Bibliography

"Screening for breast cancer: U.S. preventive services task force recommendation statement," *Annals of Internal Medicine*, vol. 151, no. 10, pp. 716–737, Nov. 2009.

S. Poplack, T. Tosteson, W. Wells, B. Pogue, P. Meaney, A. Hartov, C. Kogel, S. Soho, J. Gibson, and K. Paulsen, "Electromagnetic breast imaging: Results of a pilot studying women with abnormal mammograms," *Radiology*, vol. 243, no. 2, pp. 350–359, May 2007.

L. Sha, E. Ward, and B. Stroy, "A review of dielectric properties of normal and malignant breast tissue," in *Proc. IEEE Southeast Conf*, 2002, pp. 457–462.

P. Meaney, M. Manning, D. Li, S. Poplack, and K. Paulsen, “A clinical prototype for active microwave imaging of the breast,” *IEEE Trans. Microw. Theory Techn.* vol. 48, pp. 1841-1853, Nov. 2000.

P. M. Meaney, A. P. Gregory, N. R. Epslein, and K. D. Paulsen, “Microwave open-ended coaxial dielectric probe: interpretation of the sensing volume revised,” *BMC Medical Physics*, vol. 14, no. 3, Jun. 2014.

A. Rosen, M. Stuchly, and A. V. Vorst, “Applications of RF/Microwaves in medicine,” *IEEE Trans. Microw. Theory Techn*. vol. 50, no. 3, pp. 963–974, Mar. 2002.

X.Li, S. Davis, S. Hagness, D. van der Weide, and B. V. Veen, “Microwave imaging via space-time beamforming: Experimental investigation of tumor detection in multilayer breast phantoms,” *IEEE Trans. Microw. Theory Techn.* vol. 52, no. 8, pp. 1856–1865, Aug. 2004.

X.Li, E. Bond, B. V. Veen, and S. Hagness, “An overview of ultra-wideband microwave imaging via space-time beamforming for early-stage breast-cancer detection,” *IEEE Antennas and Propag. Mag.* vol. 47, no. 1, pp. 19–34, Feb. 2005.

E. Bond, X. Li, S. Hagness, and B. V. Veen, “Microwave imaging via space-time beamforming for early detection of breast cancer,” *IEEE Trans. Antennas and Propag*. vol. 51, no. 8, pp. 1690–1705, Aug. 2003.

J. Bourqui, M. Campbell, J. Sill, M. Shenouda, and E. Fear, “Antenna performance for ultra-wideband microwave imaging,” *IEEE Radio and Wireless Symposium (RWS 2009)*, pp. 522–525, Jan. 2009.

E. Fear and M. Stuchly, “Microwave detection of breast cancer,” *IEEE Trans. Microw. Theory. Techn.* vol. 48, no. 11, pp. 1854–1863, Nov. 2000.

E. Fear, S. Hagness, P. Meaney, M. Okoniewski, and M. Stuchly, “Enhancing breast tumor detection with near-field imaging,” *IEEE Microw. Mag.* pp. 48–56, Mar. 2002.

E. Fear, X. Li, S. Hagness, and M. Stuchly, “Confocal microwave imaging for breast cancer detection: Localization of tumors in three dimensions,” *IEEE Trans. Biomed. Eng.* vol. 49, no. 8, pp. 812–822, Aug. 2002.

A. H. Barrett and P. C. Myers. *Basic Principles and Applications of Microwave Thermography. In Medical Applications of Microwave Imaging*, Larsen, L. E., and Jacobi, J. H., Eds.; IEEE Press: New York, 1986.

L. V. Wang, X. Zhao, H. Sun, and G. Ku. “Microwave-induced acoustic imaging of biological tissues.” *Review of Scientific Instruments* vol. 70, no. 9, pp. 3744-3748, Mar. 1999.

E. Fear, J. Bourqui, , C. Curtis, D. Mew, , B. Docktor, , and C. Romano, "Microwave breast imaging with a monostatic radar-based system: a study of application to patients," *IEEE Trans. Microw. Theory Techn*, volume 61, issue 5, pp. 2119-2128, May 2013.

Y. Zhang, S. Tu, R.K. Amineh, and N.K. Nikolova, "Sensitivity-based microwave imaging with raster scanning," *IEEE MTT-S Int. Microwave Symp*., pp. 1-3, 2012.

Klemm, Maciej, Ian J. Craddock, Jack A. Leendertz, Alan Preece, and Ralph Benjamin. "Radar-based breast cancer detection using a hemispherical antenna array—experimental results." *IEEE Trans. Antennas Propag*, vol. 57, no. 6 pp. 1692-1704, Jun 2009.

N.K. Nikolova, "Microwave biomedical imaging," *Wiley Encyclopedia of Electrical and Electronics Engineering*, pp. 1–22. (published on-line Apr. 25, 2014)

N.K. Nikolova, "Microwave near-field imaging of human tissue and its applications to breast cancer detection," *IEEE Microw. Mag*., vol. 12, no. 7, pp. 78–94, Dec. 2011.

P. M. Meaney, M. W. Fanning, T. Raynolds, C. J. Fox, Q. Fang, S. P. Poplack, and K. D. Paulsen, "Initial clinical experience with microwave breast imaging in women with normal mammography," *Academic Radiology*, vol. 14, pp. 207–218, Feb. 2007.

R. K. Amineh, M. Ravan, A. Trehan, and N. K. Nikolova, “Near-field microwave imaging based on aperture raster scanning with TEM horn antennas” *IEEE Trans. Antennas Propag.,* vol. 59, no. 3, pp. 928–940, Mar. 2011.

K. Moussakhani, R.K. Amineh, and N.K. Nikolova, “High-efficiency TEM horn antenna for ultra-wide band microwave tissue imaging,” *IEEE AP-S/URSI Int. Symp. on Antennas and Propagation*, July 2011.

R. K. Amineh, K. Moussakhani, Li Liu, H. Xu, M. S. Dadash, Y. Baskharoun, and N. K. Nikolova, “Practical issues in microwave raster scanning,” European Conf. on Antennas and Propagation (EuCAP) 2011, April 2011.

K. Moussakhani, R.K. Amineh, and N.K. Nikolova, “Estimating the efficiency of antennas used as sensors in microwave tissue measurements,” *IEEE Trans. Antennas Propag*. vol. 62, no. 1, pp. 295-301, Jan. 2014.

K. Moussakhani, R.K. Amineh, and N.K. Nikolova, “Evaluating the efficiency of antennas used as sensors in microwave tissue measurements,” *IEEE AP-S/URSI Int. Symp. on Antennas and Propagation*, July 2013.

K. Moussakhani, J. McCombe, and N.K. Nikolova, “Sensitivity of microwave imaging systems employing scattering-parameter measurements,” *IEEE Trans. Microw. Theory .Techn*. (*in press*).

K. Moussakhani, J. McCombe, and N.K. Nikolova, “Sensitivity of microwave imaging systems employing scattering-parameter measurements,” *IEEE AP-S/URSI Int. Symp. on Antennas and Propagation*, July 2014.

J. Halamek, I. Viscor, and M. Kasal, “Dynamic range and acquisition system,” *Measurement Science Review* 1, no. 1, pp. 71–74, 2001.

P.S. Yarmolenko *et. al*. “Thresholds for thermal damage to normal tissues: An update” *Int. J. Hyperthermia*, vol. 27, no.4, pp. 320–343, June 2011.

R. L. Brauer, *Safety and Health for Engineers.* John Wiley, New Jersey, Hoboken, 2006.

K. McClaning and T. Vito, *Radio Receiver Design*: Noble Publishing Corporation, Atlanta, GA, 2000.

H. T. Friss,“Noise figure of radio receiver,” *Proceedings of the IRE*, vol. 32, no. 7, pp.419–422, 1944.

Agilent: Fundamentals of RF and microwave noise figure measurements, Application Note 57-1, Agilent Technologies, [Online].

H. Xu, Planar *Raster-scanning System for Near-field Microwave Imaging*. M.A.Sc. Thesis, McMaster University, 2011.

H. M. Jafari, J. M. Deen, S. Hranilovic, and N. K. Nikolova, "Co-polarised and cross-polarised antenna arrays for breast, cancer detection," *IET Microwave Antennas Propag*., vol. 1, no. 5, pp. 1055–1058, Oct. 2007.

D. A. Woten and M. El-Shenawee, "Broadband dual linear polarized antenna for statistical detection of breast cancer," *IEEE Trans. Antennas Propag*., vol. 56, no. 11, pp. 3576–3580, Nov. 2008.

R. Nilavalan, I. J. Craddock, A. Preece, J. Leendertz, and R. Benjamin, "Wideband microstrip patch antenna design for breast cancer tumour detection," *IET Microwave Antennas Propag*., vol. 1, no. 2, pp. 277–281, Apr. 2007.

H. Kanj and M. Popovic, "A novel ultra-compact broadband antenna for microwave breast tumor detection," *Progress In Electromagnetics Research, PIER* 86, pp. 169–198, 2008.

X. Li, S. C. Hagness, M. K. Choi, and D. Van Der Weide, "Numerical and experimental investigation of an ultra-wideband ridged pyramidal-horn antenna with curved launching plane for pulse radiation," *IEEE Antennas Wirel. Propag. Lett*., vol. 2, pp. 259–262, 2003.

J. Zhang, E. C. Fear, and R. Johnston, “Cross-Vivaldi antenna for breast tumor detection,” *Microwave and Opt. Lett*., vol. 51, no. 2, pp. 275–280, Feb. 2009.

R. K. Amineh, M. Ravan, A. Trehan, and N. K. Nikolova, “Near-field microwave imaging based on aperture raster scanning with TEM horn antennas,” *IEEE Trans. Antennas and Propag*., vol. 59, no. 3, pp. 928–940, Mar. 2011.

J. W. Duncan and V. P. Minerva, “100:1 bandwidth balun transformer,” Proc. Inst. Elect. Eng., vol. 48, no. 2, pp. 156–164, Feb. 1960.

P. R. Foster and S. M. Tun, “A wideband balun from coaxial line to TEM line,” *IEEE Int. Symp. Antennas and Propagation ICAP*, vol. 1, Eindhoven, The Netherlands, pp. 286–290, Apr. 1995.

G. A. Mesyats, S. N. Rukin, V. G. Shpak, and M. I. Yalandin, “Generation of high-power subsecond pulses” *Ultra-wideband Short-Pulse Electromagnetics*, vol.4, Tel-Aviv, Israel, pp1–9, Jun. 1998.

M. Lazebnik, M. Okoniewski, J. H. Booske, and S. C. Hagness, “Highly accurate Debye models for normal and malignant breast tissue dielectric properties at microwave frequencies,*”* *IEEE Microw. Compon. Lett*., vol. 17, no. 12, Dec. 2007.

Ansoft Corporation, http://www.ansoft.com.

R. K. Amineh, A. Trehan, and N. K. Nikolova, “TEM horn antenna for ultra-wide band microwave breast imaging,” *Progress In Electromagnetics Research B*, vol. 13, pp. 59–74, 2009.

M. Lazebnik, L. McCartney, D. Popovic, C. B. Watkins, M. J. Lindstrom, J. Harter, S. Sewall, A. Magliocco, J. H. Booske, M. Okoniewski,and S. C. Hagness, “A large-scale study of the ultrawide band microwave dielectric properties of normal breast tissue obtained from reduction surgeries,” *Phys. Med. Bio*l., vol. 52, pp. 2637–2656, May 2007.

A. Trehan, *Numerical and physical models for microwave breast im aging*, M.A.Sc. Thesis, McMaster University, 2009.

Emerson & Cuming Microwave Products, http://www.eccosorb.com.

Y. Zhang, S. Tu, R.K. Amineh, and N.K. Nikolova, “Sensitivity-based microwave imaging with raster scanning,” *IEEE MTT-S Int. Microwave Symp*., June 2012.

L. E. Larsen, and J. H. Jacobi, *Medical Applications of Microwave Imaging*. New York: IEEE Press, 1986.

E. Fear, X. Li, S. C. Hagness, and M. A. Stuchly, “Confocal microwave imaging for breast cancer detection: localization of tumors in three dimensions,” *IEEE Trans. Biomed. Eng.*, vol. 49, no. 8, pp. 812–822, Aug. 2002.

Z. Q. Zhang, and Q. H. Liu, “Three-dimensional nonlinear image reconstruction for microwave biomedical imaging,” *IEEE Trans. Biomed*. Eng., vol. 51, no. 3, pp. 544–548, Mar. 2004.

T. Rubaek, P. M. Meaney, P. Meincke, and K. D. Paulsen, “Nonlinear microwave imaging for breast-cancer screening using Gauss–Newton’s method and the CGLS inversion algorithm,” *IEEE Trans. Antennas Propag*., vol. 55, no. 8, pp. 2320–2331, Aug. 2007.

R. Maaskant, D. J. Bekers, M. J. Arts, W. A. van Cappellen, and M. V. Ivashina “Evaluation of the radiation efficiency and the noise temperature of low-loss antennas,” *IEEE Antennas Wireless Propag*. Lett., vol. 8, pp. 1536−1225, Nov. 2009.

H. Kanj and M. Popovic, “Miniaturized microstrip-med “dark eyes” antenna for near-field microwave sensing,” IEEE Antennas Wireless Propag. Lett., vol. 4, pp. 397–401, 2005.

“IEEE standard definitions of terms for antennas,” IEEE Std 145-1993, p. i, 1993.

H. A. Wheeler, “The radiansphere around a small antenna,” *Proc. IRE*, vol. 47, no. 8, pp. 1325−1331, Aug. 1959.

S. Agahi and W. Domino, “Efficiency measurements of portable-handset antennas using the Wheeler cap,” *Applied Microwave & Wireless*, vol. 12, pp. 34–42, Jun. 2000.

H. Schantz, *The Art and Science of UWB Antennas*. Norwood, MA: Artech House, 2005, ISBN: 1-58053-88-6.

G. L. Fur, C. Lemoine, P. Besnier, and A. Sharaiha, "Performances of UWB Wheeler Cap and reverberation chamber to carry out efficiency measurements of narrowband antennas," *IEEE Antennas Wireless Propag. Lett.*, vol. 8, pp. 332–335, 2009.

M. Huynh, *Wideband Compact Antennas for Wireless Communication Applications*. Ph.D. Thesis, Virginia State Univ., 2004.

Y. Huang, Y. Lu, S. Boyes, H. T. Chattha, and N. Khiabani, "Wideband antenna efficiency measurements," *IEEE International Workshop on Antenna Technology* (iWAT) 2010, Lisbon.

C. A. Balanis, *Antenna Theory: Analysis and Design*. New York: Harper and Row, 1982.

C. L. Holloway, H. Shah, R. J. Pirkl, W. Young, D. A. Hill, and J. Ladbury, "New reverberation chamber techniques for determining the radiation and total efficiency of antennas," *IEEE Trans. Antennas Propag.*, vol. 60, no. 4, pp. 1758–1770, Apr. 2012.

R. H. Johnston and J. G. McRory, "An improved small antenna radiation-efficiency measurement method," *IEEE Antennas Propag. Mag*., vol. 40, no. 5, pp. 40–48, Oct. 1998.

Matlab7.1 ed. Natick, MA, The MathWorks, Inc., 2005.

T. Bilnder, C. Heitzinger, and S. Selberherr, “A study on global and local optimization techniques for TCAD analysis tasks,” *IEEE Trans. Computer-aided Des. Integr. Circuits Syst*., vol. 23, no. 6, Jun. 2004.

T. A. El-Mihoub, A. A. Hopgood, L. Nolle, and A. Battersby, ‘‘Hybrid genetic algorithms: a review,’’ *Engineering Letters*, vol. 3, no. 2, pp. 124–137, Aug. 2006.

P. Preux and E.-G. Talbi, “Towards hybrid evolutionary algorithms,” *International Transactions in Operational Research*, vol. 6, no.6, pp. 557–570, Nov. 1999.

Ansoft Corporation [Online]. Available: http://www.ansoft.com

M.S. Dadash, K. Moussakhani, and J.J. McCombe, “Quad-ridge horn antenna for tissue measurements,” *Computational Electromagnetics Res. Lab., McMaster University, CEM-R-69*, June 2014.